Ice particle morphology and microphysical properties of cirrus clouds inferred from combined CALIOP-IIR measurements: Ice crystals in cirrus clouds

Article *in* Journal of Geophysical Research Atmospheres · April 2017

DOI: 10.1002/2016JD026080

AGU PUBLICATIONS

JGR

Journal of Geophysical Research: Atmospheres

RESEARCH ARTICLE

10.1002/2016JD026080

Key Points:

- Cirrus cloud particle morphology is inferred from satellite measurements with an optimal estimation
- The retrievals are validated with multiple satellite products on a pixel-by-pixel basis
- The lidar ratio is affected by horizontally oriented particles where the temperature is greater than −40°C

Correspondence to:
M. Saito,
masanori.saito.p4@dc.tohoku.ac.jp

Citation:
Saito, M., H. Iwabuchi, P. Yang, G. Tang, M. D. King, and M. Sekiguchi (2017), Ice particle morphology and microphysical properties of cirrus clouds inferred from combined CALIOP–IIR measurements, *J. Geophys. Res. Atmos., 122*, doi:10.1002/2016JD026080.

Received 12 OCT 2016
Accepted 31 MAR 2017
Accepted article online 10 APR 2017

Ice particle morphology and microphysical properties of cirrus clouds inferred from combined CALIOP-IIR measurements

Masanori Saito[1], Hironobu Iwabuchi[1], Ping Yang[2], Guanglin Tang[2], Michael D. King[2,3], and Miho Sekiguchi[4]

[1]Department of Geophysics, Graduate School of Science, Tohoku University, Sendai, Japan, [2]Department of Atmospheric Sciences, Texas A&M University, College Station, Texas, USA, [3]Laboratory for Atmospheric & Space Physics, University of Colorado Boulder, Boulder, Colorado, USA, [4]Department of Marine Electronics and Mechanical Engineering, Tokyo University of Marine Science and Technology, Tokyo, Japan

Abstract Ice particle morphology and microphysical properties of cirrus clouds are essential for assessing radiative forcing associated with these clouds. We develop an optimal estimation-based algorithm to infer cirrus cloud optical thickness (COT), cloud effective radius (CER), plate fraction including quasi-horizontally oriented plates (HOPs), and the degree of surface roughness from the Cloud Aerosol Lidar with Orthogonal Polarization (CALIOP) and the Infrared Imaging Radiometer (IIR) on the Cloud Aerosol Lidar and Infrared Pathfinder Satellite Observation (CALIPSO) platform. A simple but realistic ice particle model is used, and the relevant bulk optical properties are computed using state-of-the-art light-scattering computational capabilities. Rigorous estimation of uncertainties related to surface properties, atmospheric gases, and cloud heterogeneity is performed. The results based on the present method show that COTs are quite consistent with other satellite products and CERs essentially agree with the other counterparts. A 1 month global analysis for April 2007, in which CALIPSO off-nadir angle is 0.3°, shows that the HOP has significant temperature-dependence and is critical to the lidar ratio when cloud temperature is warmer than −40°C. The lidar ratio is calculated from the bulk optical properties based on the inferred parameters, showing robust temperature dependence. The median lidar ratio of cirrus clouds is 27–31 sr over the globe.

1. Introduction

Cirrus clouds cover 20% of the globe and play an essential role in Earth's climate system [*Liou and Yang*, 2016]. The radiative effects of cirrus clouds greatly depend on their optical and microphysical properties such as cloud optical thickness (COT) and cloud-particle effective radius (CER) [*Hong et al.*, 2009] as well as their particle morphology [*Key et al.*, 2002; *Yi et al.*, 2013], which could even switch their radiative effects between net cooling and warming effects on the atmosphere [*Stephens et al.*, 1990]. Accurate estimation of global average radiative effects is still challenging, partly because optical and microphysical properties of cirrus clouds are not well known. Aircraft measurements in cirrus clouds served as a constraint on the properties [*Heymsfield et al.*, 2013]. However, reliability of in situ measurements of small ice crystals, to which cloud radiative effects are very sensitive, is rather questionable due to potential ice shattering on probe inlets [*Field et al.*, 2003; *Lawson*, 2011], and the number of aircraft-based measurements is quite limited due to the expense of the measurements.

Various satellite cloud remote sensing instruments have provided a vast amount of information in recent decades. Numerous techniques have been developed to infer cloud optical and microphysical properties from measurements by individual instruments such as passive and active sensors [*Inoue*, 1987; *Nakajima and King*, 1990; *Parol et al.*, 1991; *Vaughan et al.*, 2004]. Particularly, passive thermal infrared (TIR) radiometric measurements are sensitive to optically thin clouds [*Cooper and Garrett*, 2010], and active lidar measurements can supply vertical structure and geometric information in transparent clouds [*Sassen et al.*, 2008], thereby giving us new perspectives on cirrus clouds over the globe.

However, several possible sources of errors and biases on those products have been reported. With passive radiometric measurements, cloud reflectivity in visible and near-infrared wavelengths is strongly influenced by cloud heterogeneity and the assumed ice particle texture, leading to systematic biases as well as angle-geometry-dependent local biases on both COT and CER retrievals [*Várnai and Marshak*, 2007; *Yang et al.*, 2008]. In TIR wavelengths, although impacts of ice particle morphology on the signals are small, the cloud heterogeneity effect still exists and is not negligible [*Fauchez et al.*, 2015]. Moreover, any multilayer cloud system induces further biases on a retrieval quantity [*Chang and Li*, 2005] due to the single-layer approximation used in the vast majority of retrieval techniques. With active lidar measurements, vertical profiles of extinction coefficient (namely, layer-COT profiles) are obtained by solving the lidar equation, which needs prior knowledge of the extinction-to-backscatter ratio, or the so-called lidar ratio, in the cirrus cloud [*Young and Vaughan*, 2009]. Accuracy of the COT retrievals hinges on quantitative reliability of the lidar ratio, which has, however, substantial variability over the particle morphology. Current knowledge of the morphological parameters of ice crystals in clouds is poor and quite limited. Furthermore, the presence of quasi-horizontally oriented plate crystals (hereinafter referred to as HOP) in cirrus clouds provides specular reflection, resulting in strong backscattering even if the fraction of such particles is a few percent [e.g., *Sassen and Benson*, 2001]. This is a significant obstacle for obtaining accurate COT retrievals from lidar measurements. As a result, intercomparisons among the retrievals with different techniques do not show good agreement [*Holz et al.*, 2016], which complicates our understanding of cirrus radiative effects. Further efforts to implement more realistic ice particle morphologies and more representative cloud-atmosphere uncertainties in retrieval techniques are needed.

Most knowledge of ice particle morphology is based on laboratory experiments [*Bailey and Hallett*, 2004; *Pfalzgraff et al.*, 2010; *Magee et al.*, 2014] and aircraft in situ measurements [*Lawson et al.*, 2006; *Ulanowski et al.*, 2014]. Measurements imply that ice particles are a mixture of ice particles with complex morphologies (e.g., column aggregates and irregular polycrystals) and pristine crystals (e.g., hexagonal plate and column), and their fractions strongly depend on temperature and ice supersaturation. Since satellite polarimetric measurements became available, global averages of ice particle morphological parameters have been investigated, and results imply that roughened particles are more realistic than unroughened (smooth) particles [*Baran and Labonnote*, 2006; *Cole et al.*, 2013; *Holz et al.*, 2016; *Platnick et al.*, 2017] and that a column aggregate crystal shape is most representative in ice clouds over the globe [*Guignard et al.*, 2012; *Cole et al.*, 2014]. Satellite lidar measurements reveal that the population of HOP crystals is relatively large where air temperature is about −20°C [*Yoshida et al.*, 2010]. Recently, several novel approaches have been developed to enable pixel-by-pixel inference of ice particle surface roughness in optically thick ice clouds (generally, $\tau > \sim 5$) [*van Diedenhoven et al.*, 2012; *Hioki et al.*, 2016], but available information of morphological parameters in optically thin clouds is very limited.

The overarching goal of this paper is to improve understanding of particle morphology and microphysical properties in optically thin cirrus clouds. Since 2002, NASA has had a constellation of satellites on the same orbit, which is referred to as the A-Train [*Stephens et al.*, 2002]. The A-train constellation makes it possible to design algorithms that use multiple measurements at the pixel level. A combination of instruments can enhance the total information content by compensating for the limitations of each of the instruments. *Delanoë and Hogan* [2010] provided the DARDAR product that contains vertical profiles of extinction coefficient and CER inferred from combined lidar, radar, and TIR measurements. Two backscattering profiles from both lidar and radar allowed inferences of vertical profiles of not only the extinction coefficient but also CERs in opaque ice clouds, and TIR brightness temperatures (BTs) help to constrain both parameters where radar signals are lost, improving accuracy of the retrievals. In addition, optimal estimation is a useful approach to solve inversion problems based on the Bayesian theorem by taking account of uncertainties in the signals and using prior knowledge to improve the retrievals [*Rodgers*, 2000]. Recent efforts permit more accurate retrievals of ice cloud microphysical properties by taking into account multilayer clouds [e.g., *Sourdeval et al.*, 2015] and rigorously evaluated uncertainties associated with atmospheric gases and cloud properties [e.g., *Wang et al.*, 2016]. Further treatment of uncertainties and relaxation of assumptions in algorithms possibly make retrieval accuracy better and can tackle obstacles to infer particle morphology in optically thin clouds. This paper demonstrates a method to infer ice water path (IWP), CER, surface temperature (T_{SFC}), and two morphological parameters (plate fraction (F_{PLT}) and surface roughness of ice crystal aggregates (σ^2_{POLY})) in a cirrus cloud simultaneously from combined passive TIR and active lidar measurements on a pixel-by-pixel basis by assuming a simple ice model that is a mixture of pristine hexagonal plates and aggregates. The lidar ratio, HOP fraction, and COT are also derived in addition to the inferred parameters. Uncertainties associated with measurement signals, atmospheric gases, surface properties, and cloud heterogeneity are taken into account in the algorithm.

Table 1. Data Used in the Method

Data	Products	Spatial Resolution	Temporal Resolution
Measurements	CALIOP L2 CLay	1 km	—
Measurements	IIR L2 Track	1 km	—
Sea surface temperature	MODIS L3	0.4167°	8 day mean
Land surface temperature	MODIS L3	0.05°	8 day mean
Land surface emissivity	BFED	0.05°	Monthly
Atmospheric profile	MERRA	1.25°, 42 level	3 h
Trace gas concentration	Climatology	Global	Monthly

This paper is organized into the following sections: Section 2 describes detailed methodologies and data used in the algorithm. Section 3 discusses methods of uncertainty evaluation. Section 4 provides results including retrieval error analysis, various validations, and a 1 month global analysis. Conclusions and future prospects are given in section 5.

2. Methodologies

The basic principle of an optimal estimation-based algorithm is to find a solution that best fits the physical model to the measurements under constraints of prior knowledge about the climatology of inference parameters. In this section, first, the data and criteria for the method are explained. Next, forward models for both TIR BT and lidar signals are briefly described. Finally, the optimal estimation method for the inferences is given.

2.1. Data and Criteria

In this study, various data sources are used to handle realistic atmosphere-cloud conditions in the retrieval algorithm as summarized in Table 1.

The Cloud Aerosol Lidar and Infrared Pathfinder Satellite Observation (CALIPSO) has been in orbit since 2006 [*Winker et al.*, 2009]. The Cloud Aerosol Lidar with Orthogonal Polarization (CALIOP) on the CALIPSO platform yields vertical profiles of backscattering intensity at the two wavelengths: 532 nm and 1064 nm. Moreover, the 532 nm channel, especially, has polarization capabilities for measuring the parallel and perpendicular radiation components. The CALIOP level 2 cloud layer 1 km products (L2 CLay 1 km) in version 3.01 provides the layer-integrated total attenuated backscatter (IAB) and the depolarization ratio (DPR) at 532 nm defined as

$$\mathrm{IAB} = \int_{\mathrm{CTH}}^{\mathrm{CBH}} \frac{\beta'_{\perp}(z) + \beta'_{\parallel}(z)}{\cos\theta_{\mathrm{offndr}}} \mathrm{d}z \tag{1}$$

and

$$\mathrm{DPR} = \frac{\int_{\mathrm{CTH}}^{\mathrm{CBH}} \beta'_{\perp}(z)\mathrm{d}z}{\int_{\mathrm{CTH}}^{\mathrm{CBH}} \beta'_{\parallel}(z)\mathrm{d}z}, \tag{2}$$

where $\beta'_{\parallel}(z)$ and $\beta'_{\perp}(z)$ are the parallel and perpendicular components of attenuated backscatter signals as functions of altitude z, respectively; θ_{offndr} is the off-nadir angle of the CALIOP pointing direction, and CTH and CBH are cloud top height and cloud base height, respectively. The IAB and DPR are sensitive to HOPs, since specular reflection causes strong backscattering and does not change polarization characteristics, namely, causing a large IAB and low DPR. In addition to the two signals, CTH, CBH, and thermodynamic phase are obtained from the L2 CLay 1 km product (shown near the end of this section). Another instrument on board CALIPSO is the Imaging Infrared Radiometer (IIR), providing BTs at three channels in the split window wavelengths: 8.65, 10.6, and 12.05 μm. The BTs (referred to as $\mathrm{BT}_{8.65}$, $\mathrm{BT}_{10.6}$, and $\mathrm{BT}_{12.05}$) have different characteristics in ice absorption, making it feasible to infer both COT and CER from the split window bands. The IIR L2 Track product contains those three BTs on the CALIOP collocated track with a 1 km resolution, which permits synergetic use of the CALIOP and IIR product easily.

For surface and meteorological properties, this study follows *Iwabuchi et al.* [2016] (hereinafter referred to as I16) that uses multiple products and data, such as sea surface temperature/emissivity (SST/SSE), land surface

Table 2. Pixel Data Criteria

Source	Quantity	Threshold
L2 CLay 1 km	Cloud phase	Ice or oriented ice crystals
L2 CLay 1 km	Cloud layer	Single
L2 CLay 1 km	Cloud top height	>6 km
L2 CLay 5 km	Opacity flag	Transparent

temperature/emissivity (LST/LSE), and vertical profiles of temperature and atmospheric gases, to apply the analysis to the globe. The Moderate Resolution Imaging Spectroradiometer (MODIS) 8 day mean level 3 (L3) product provides SST and LST with a root-mean-square error (RMSE) about 0.35 – 0.4 K and less than 1 K [*Brown et al.*, 1999; *Wan and Li*, 1997]. The LSE is from the Baseline-Fit Emissivity Database (BFED) monthly product that guarantees a RMSE less than 0.01 [*Seemann et al.*, 2008]. Atmospheric profiles including air temperature and ozone and water vapor mixing ratios are obtained from the Modern-Era Retrospective analysis for Research and Applications (MERRA) product [*Rienecker et al.*, 2011]. Concentrations of carbon dioxide (CO_2), methane (CH_4) and nitrous oxide (N_2O) are set to global monthly mean values provided by the World Data Center for Greenhouse Gases from the World Meteorological Organization Global Atmosphere Watch program [*Tsutsumi et al.*, 2009].

To select CALIOP-IIR collocated pixels (hereinafter referred to as “pixels”) containing single-layer ice clouds, we use CTH, the feature classification flag, and the opacity flag available in CALIOP L2 CLay 1 km and 5 km products. The data criteria are summarized in Table 2.

On the feature classification flag, cloud thermodynamic phase is determined on the basis of a relationship between backscattering intensity and depolarization ratio in addition to spatial coherence in both parameters, determining “ice,” “water,” and “oriented ice crystals” for each layer [*Hu et al.*, 2009]. We use pixels determined as ice or oriented ice crystals for the analysis. In addition, the L2 CLay 1 km product shows the number of cloud layers for each pixel; thus, single-layer clouds can be selected. Note that pixels containing a multilayer cloud system with vertical distance between two clouds less than 1.5 km are treated as a single-layer cloud to increase data availability. This study neglects the cloud layers detected with a horizontal average of 5 to 80 km stored in the L2 CLay 5 km product since these clouds are optically very thin and have only a slight impact on TIR radiance, which will be discussed in section 3. Furthermore, the L2 CLay 5 km product has an opacity flag that tells us if the cloud is transparent. CALIOP data for a transparent cloud guarantee reliability of the CBH estimation.

2.2. Forward Models

A simple but realistic ice model is needed to calculate the bulk optical properties used for solving the radiative transfer equation. The ice model in this study is assumed to be a mixture of hexagonal plates and aggregates based on *Bailey and Hallett* [2004]. The plate fraction is defined as the number fraction of hexagonal plates over all crystals. In natural cirrus clouds, hexagonal plates are likely to have quasi-horizontal orientations with small fluctuations of the tilting angle when the maximum diameter of the plate is greater than 100 μm, according to lidar observations [*Sassen*, 1980] as well as theoretical simulations [*Bréon and Dubrulle*, 2004]. We assume that hexagonal plates smaller (larger) than 100 μm are randomly (quasi-horizontally) oriented according to *Klett* [1995]. The degree of surface roughness in conjunction with the hexagonal plates is assumed to be 0 (smooth particle). The aspect ratio and tilting angle of HOP have significant impacts on the single-scattering properties [*Noel and Chepfer*, 2004; *Zhou et al.*, 2012]. The aspect ratios of plate crystals were investigated by aircraft in situ measurements [*Pruppacher and Klett*, 1997], providing a parameterization as $2\frac{a}{L} = 0.8038a^{0.5206}$, where a and L are the semiwidth and length of a hexagonal plate crystal. Variation of the tilting angle is generally assumed to have a Gaussian distribution based on ground- and satellite-based polarimetric measurements [*Noel and Chepfer*, 2004; *Noel and Sassen*, 2005]. *Bréon and Dubrulle* [2004] showed the cumulative density distribution of the tilting angle of HOPs based on satellite polarimetric measurements as well as aerodynamic simulations, implying that most HOPs have a tilting angle less than 1.0° in all clouds but greater than 0.5° particularly in high clouds. In this study, the tilting angle variation of HOP follows findings by Bréon’s work [see *Bréon and Dubrulle*, 2004, Figure 9] that shows a lognormal distribution of tilting angle with average and sigma value of ln 0.9° and 0.6° over ice clouds when cloud top pressure (CTP) ranges from 100 to 500 hPa. Moreover, we use the column aggregate shape model because previous studies imply that this ice particle shape shows maximum consistency between observations and simulations in ice cloud reflectance on a global scale [*Guignard et al.*, 2012; *Cole et al.*, 2014]. The column aggregate model assumes several degrees of surface roughness (0.001 to 0.7) defined by *Yang and Liou* [1998].

The single-scattering properties of ice crystals are calculated with state-of-the-art light scattering computational capabilities. Including the interference effect in the light scattering compilation is essential to obtain accurate scattering properties around the 180° backward direction for HOP [*Borovoi and Grishin*, 2003]. The Physical Geometric Optics Hybrid (PGOH) [*Bi et al.*, 2011] is feasible for calculating the optical properties of oriented particles and is applicable for intermediate and large ice crystals, whereas the Improved Geometric Optics Method (IGOM) [*Yang and Liou*, 1996; *Bi et al.*, 2010] is much more time efficient for random-oriented particles and is more accurate than conventional ray tracing methods. In PGOH, the only approximation made is that the rays follow the geometric optics scheme. Therefore, the light scattering computation for HOP at 532 nm is performed with PGOH, and we also use the latest version of IGOM to obtain single-scattering properties of randomly oriented hexagonal plates at 532 nm and column aggregates in the 532 nm and TIR bands. In addition to the IGOM, a backscattering correction based on *Zhou and Yang* [2015] for column aggregates is performed to calculate optical properties in visible wavelengths, providing more realistic backscattering properties [*Ding et al.*, 2016]. A detailed explanation of the correction is given in the appendix. Using these single-scattering properties, the bulk optical properties are calculated by assuming a Gamma distribution with a parameterization provided by *Iwabuchi et al.* [2012]. The lidar ratio (S) is calculated from the bulk optical properties as

$$S = \frac{4\pi}{\omega P_{11}(\pi)}. \tag{3}$$

where ω and P_{11} are the single scattering albedo and the scattering phase function, respectively.

In TIR forward modeling, we use the TIR radiative transfer simulator originally developed by I16 and adjusted to the IIR spectral bands. The radiative transfer equation is solved by the two-stream approximation [*Nakajima et al.*, 2000] in conjunction with the delta-M method [*Wiscombe*, 1977] by assuming a plane parallel atmosphere. The forward model uses atmosphere and surface properties obtained from the source data described in the previous subsection. The correlated k distribution (CKD) method with five quadrature points for each band [*Sekiguchi and Nakajima*, 2008] is used to compute absorption optical properties associated with clouds and atmospheric gases (water vapor, carbon dioxide, ozone, nitrous oxide, carbon monoxide, and methane). Finally, the forward model calculates the band-mean TIR radiance by integration over the CKD quadratures and converts the BT for each band by Akima interpolation [*Akima*, 1970] from a precalculated radiance-BT look-up table (LUT). Systematic biases associated with approximations in the radiative transfer equations are evaluated through comparison with an accurate radiative transfer model, RSTAR [*Nakajima and Tanaka*, 1986, 1988], which is based on the matrix-operator method and discrete ordinate method [*Chandrasekhar*, 1960]. Cubic polynomials with coefficients given by the comparison correct the BT for each band. Plane parallel homogeneous (PPH) cloud properties are assumed, and cloud boundaries are given from the CALIOP in the forward model. Note that we do not take into account plate crystals on the bulk optical properties over TIR wavelengths due to three reasons: (1) Particle texture does not have a significant effect on TIR radiance [*Cooper et al.*, 2006], (2) the fraction of plates is expected to be small, and (3) ignoring oriented particles dramatically simplifies the radiative transfer equation. In addition, a column aggregate for TIR simulation is assumed to have a severely roughened surface (σ^2_{POLY}) for simplification. Errors associated with this assumption will be discussed in the next section.

In lidar backscattering simulations at 532 nm, we use the Monte Carlo radiative transfer simulator [*Hu et al.*, 2001; *Zhou et al.*, 2012]. The photon propagation direction is determined by the two-dimensional phase function (scattering zenith and azimuth angle on a scattering plane) that depends on the photon incident angle given from the LUT of the bulk optical properties. PPH cloud properties are assumed in the forward model. Sensitivity tests indicate that simulated IAB and DPR are not sensitive to cloud geometrical thickness. Thus we assume that the cloud geometrical thickness is 2 km and do not use CBH from the CALIOP. The simulator neglects the scattering of molecules and gases because the effects of those types of scattering in a cloud layer are negligibly small. To guarantee the accuracy of simulations, we set the number of photons to be 10^8 and calculate the RMSE of simulated IAB and DPR simultaneously. Once we specify IWP, CER, the plate fraction, and the surface roughness, the model provides not only IAB, DPR, and those RMSEs but also COT, the lidar ratio, and the fraction of HOP. To reduce computational burden in real-time processing, the signals are precalculated for input values and tabulated in a LUT.

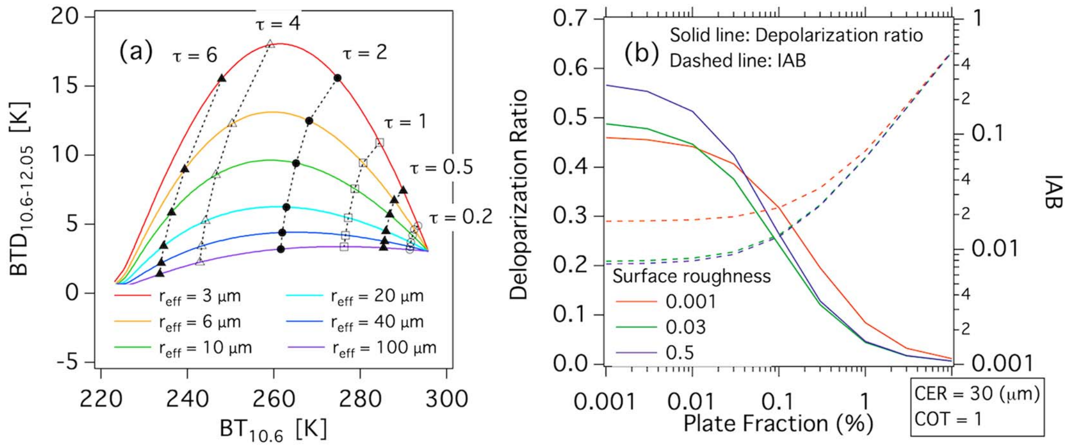

Figure 1. Sensitivities of (a) TIR bands to COT and CER and (b) lidar signals to the plate fraction and surface roughness. Horizontal axis shows the brightness temperature (BT) in the 10.6 μm band. Vertical axis shows the BT difference between 10.6 μm and 12.05 μm. Cloud top (base) height is assumed to be 12 (10) km, and the ice particle model is a column aggregate shape with severely roughened surface. The lidar signals are simulated by assuming COT = 1 and CER = 30 μm.

Figure 1 shows sensitivity tests of TIR and lidar signals to the cloud properties. The COT at 532 nm is used throughout this paper. The lidar off-nadir angle is assumed to be 0.3°. Figure 1a shows that the IIR BT and the differences between bands are sensitive to COT and CER in case of COT of 0.2 or more and the signals are more sensitive to those properties when CER is small. The lidar signals are sensitive to the plate fraction, as shown in Figure 1b. These signals have relatively small but nonnegligible sensitivity to surface roughness, especially when clouds contain few plate particles. Clouds with a large plate fraction contain many HOPs, to which both IAB and DPR are sensitive. The low-surface roughness particles have simpler surface texture and intensify backscattering, resulting in large IAB and small DPR, but severely roughened particles increase DPR and decrease IAB.

2.3. Inversion Theory

Optimal estimation [*Rodgers*, 2000] solves an inversion problem, by estimating a state vector under the constraint of prior information in the state vector. The strength of the constraint is given by the standard deviation of the a priori probability density. Determination of a priori estimates and errors is discussed extensively below and in section 3. If a state vector element varies over several orders of magnitude, the logarithm of that variable converges quickly.

The measurement vector is

$$\mathbf{y} = \begin{pmatrix} \mathrm{BT}_{8.65} \\ \mathrm{BT}_{10.6} \\ \mathrm{BT}_{12.0} \\ \mathrm{IAB} \\ \mathrm{DPR} \end{pmatrix}, \tag{4}$$

and the state vector is

$$\mathbf{x} = \begin{pmatrix} \ln \mathrm{IWP} \\ \ln r_{\mathrm{eff}} \\ T_{\mathrm{sfc}} \\ \ln F_{\mathrm{PLT}} \\ \ln \sigma^2_{\mathrm{POLY}} \end{pmatrix}. \tag{5}$$

The equation to be solved is

$$\mathbf{y} = \mathbf{F}(\mathbf{x}, \mathbf{b}) + \mathbf{e}, \tag{6}$$

where $\mathbf{F}(\mathbf{x}, \mathbf{b})$ is the simulated measurement, $\mathbf{b}$ is a model parameter vector, and $\mathbf{e}$ are the simulated measurement and the measurement-model error. The cost function (J) for optimal estimation is

$$J = [\mathbf{y} - \mathbf{F}(\mathbf{x}, \mathbf{b})]^T \mathbf{S}_{\mathbf{e}}^{-1} [\mathbf{y} - \mathbf{F}(\mathbf{x}, \mathbf{b})] + [\mathbf{x} - \mathbf{x}_{\mathbf{a}}]^T \mathbf{S}_{\mathbf{a}}^{-1} [\mathbf{x} - \mathbf{x}_{\mathbf{a}}], \tag{7}$$

Table 3. Prior Information in the State Vector

Variable	A Priori	Sigma Value	Minimum Value	Maximum Value
ln IWP (kg/m^2)	ln 0.01	4.6	$\tau = 0.03$	$\tau = 10.0$
ln r_{eff} (μm)	ln 30	1.0	ln 5	ln 100
T_{sfc} (K)	$T_{\mathrm{sfc,MODIS}}$	0.7/3.0 for ocean/land	$T_{\mathrm{sfc,MODIS}} - 3\sigma$	$T_{\mathrm{sfc,MODIS}} + 3\sigma$
ln F_{PLT} (%)	ln 0.1	4.6	ln 0.001	ln 10.0
ln σ^2_{POLY}	ln 0.03	4.6	ln 0.001	ln 0.7

where $\mathbf{x_a}$ is the a priori vector, $\mathbf{S_a}$ is the error covariance matrix of $\mathbf{x_a}$, and $\mathbf{S_e}$ is the model-measurement error covariance matrix. The prior values and the standard deviation of a priori used here are summarized in Table 3.

The prior IWP is set as 0.01 kg/m^2 with a weak constraint and a specified maximum/mimimum COT range. CER is set to a climatological value as a priori with moderate uncertainty. The a priori surface temperature is variable here and is given by MODIS LST ($T_{\mathrm{sfc,MODIS}}$) with a strong constraint that assumes RMSEs of 0.7 (3) K for SST (LST) as used by I16. The surface temperature is important for retrievals in an optically thin cloud. If MODIS L3 product has bias, the inferred cloud microphysical properties are biased, but taking account of the uncertainty in the surface temperature can reduce this bias. Since there is little prior knowledge of the plate fraction and degree of surface roughness, these a priori values are set as 0.1% and 0.03 (moderate surface roughness), around the middle values of the expected range, and large uncertainty is allowed. To minimize the cost function, the Levenberg-Marquardt Method is used. A solution with cost function $J \leq 10$ is defined as an optimal solution in this study.

3. Bias and Uncertainty Evaluations

Overall, the quality of retrievals depends on how accurate the model-measurement error is evaluated. Overestimation of the error loses information content from measurements and leads to systematic biases of retrievals, and underestimation of the error potentially leads to errors in retrievals. In addition, errors associated with cloud-atmosphere properties may have significant correlation among measurement signals. Furthermore, measurement biases caused by gradual degradation of sensors over several years causes systematic but probably small biases.

I16 uses a novel approach to evaluate cloud-surface-atmosphere uncertainty. In this study, we evaluate uncertainty associated with cloud heterogeneity at the subpixel level in addition to surface properties, atmospheric profiles, forward modeling, and measurement noise as well as biases. The measurement-model covariance matrix is represented as

$$\mathbf{S_e} = \mathbf{K_{SFC}} \mathbf{S_{e,SFC}} \mathbf{K}^T_{\mathbf{SFC}} + \mathbf{S_{e,ATM}} + \mathbf{S_{e,FWD}} + \mathbf{S_{e,MEAS}} + \mathbf{S_{e,CH}}, \tag{8}$$

where $\mathbf{S_{e,SFC}}$ and $\mathbf{K_{SFC}}$ are the covariance and Jacobian matrices with respect to surface emissivity, and $\mathbf{S_{e,ATM}}$, $\mathbf{S_{e,FWD}}$, $\mathbf{S_{e,MEAS}}$, and $\mathbf{S_{e,CH}}$ are the covariance matrix with respect to atmospheric profiles, forward modeling, measurement noise, and cloud heterogeneity, respectively. The TIR signals are affected by all error sources, but the lidar measurements may not be affected by uncertainty in surface emissivity, atmospheric profiles, or cloud heterogeneity since those properties do not contribute to the lidar signals in the upper troposphere. Therefore, the variance of the lidar signals and the covariance of the lidar and TIR signals associated with the three error sources are assumed to be zero.

Surface emissivity for each band has an impact on the retrievals if the cloud is optically thin. The uncertainty in surface emissivity is quantified by modeling. The forward model calculates the $\mathbf{K_{SFC}}$ matrix, whose elements are SSE/LSE for each TIR band. *Newman et al.* [2005] estimates the RMSE of uncertainty in SSE to be 0.001 when the viewing zenith angle is less than 60°. The uncertainty in LSE is evaluated by taking into account uncertainty in the BFED product, uncertainty in the MODIS day-night algorithm and error propagation though linear interpolation. The estimated RMSE of LSE is about 0.002–0.025 at the TIR bands.

The uncertainties in atmospheric profiles include uncertainties of temperature and mixing ratios of gases. I16 has evaluated the uncertainty in those properties using MERRA data set. In I16, error vertical profiles of those properties are simplified by parameterization with eight coefficients. An error covariance matrix obtained from MODIS measurements over clear-sky pixels is compared with the simulated error covariance matrix under clear-sky conditions by specifying the eight coefficients randomly. The best coefficients are obtained by minimizing the sum of residuals for each element of the matrix. The coefficients reconstruct the global-mean error vertical profiles of those properties. In this study, the error profiles are used to evaluate the uncertainty in atmospheric profiles for cloudy cases. As a result, the RMSEs associated with the uncertainty of atmospheric profiles are 0.6 K at 8.65 μm and 10.6 μm and 1 K at 12.05 μm, and correlation coefficients among the bands is ~ 0.9.

Uncertainty in IIR forward modeling is evaluated by comparison with the RSTAR radiative transfer model [*Nakajima and Tanaka*, 1986, 1988]. A two-stream approximation may have biases when the scattering contribution is large, and the bias should depend on scattering properties of clouds. Thus, the error covariance matrix in forward modeling is evaluated by comparison between simulated TIR signals from the two models. The error variance reaches 0.2 (0.1) K^2 at 8.65 μm when the CER is less (greater) than 20 μm, and other elements including variance and covariance are below 0.03 K^2. The uncertainty in the lidar signal simulator is evaluated by simulating Monte Carlo noise.

In measurement uncertainty, we assume that measurement noise has no correlation among all elements of the measurement vector. Measurement uncertainty in IIR is caused by measurement signal noise, calibration biases, and uncertainty. The IIR sensor is composed of a cooled microbolometer, and these uncertainties vary with observed BT as 0.2, 0.27, and 0.19 K at 8.65, 10.6, and 12.05 (μm) for 210 K, and 0.09, 0.14, and 0.11 for 250 K, according to tests that took place before the launch [*Garnier et al.*, 2012]. The measurement noise is obtained by linear interpolation from the values when the observed BT is within the range. When the BT is greater (smaller) than 250 (210) K, we assume the noise to be the same as at 250 (210) K. The CALIOP L2 CLay 1 km product contains estimated uncertainties of IAB and DPR, and this study uses those uncertainties at the measurement noise of CALIOP signals. Measurement biases in IIR signals are corrected based on a model-measurement comparison over the globe in clear-sky conditions over a week called the "TEST" week centered at the vernal equinox day in 2007. Since the clear-sky diagnosis in this study is based on the CALIOP L2 CLay 1 km product, some clear-sky pixels are contaminated by clouds detected with a horizontal average of 5 to 80 km. According to the CALIOP CLay 5 km product and the forward model calculations, 13.9% of the clear-sky pixels are contaminated by optically thin clouds with the median COT of 0.019, and these clouds affect the measurement bias correction by 0.03 K that is significantly smaller than those from other factors.

Evaluation of cloud heterogeneity at the subpixel scale is quite challenging. The uncertainty due to cloud heterogeneity is evaluated with several simplifications in uncertainty modeling. Cloud heterogeneity leads to not only noise-like uncertainty but also biases in observed TIR signals. *Fauchez et al.* [2014] showed that cloud heterogeneity, which is well correlated with the variance of subpixel COT, leads to substantial biases of TIR signals, and uncertainty that has a distribution centered at the bias, with magnitudes depending on COT. This study treats the uncertainty as a noise distribution assuming a Gaussian distribution but assumes the bias to be zero because it is difficult to quantify subpixel variability of COT from TIR signals at the pixel level. This is beyond the scope of the paper and is left for future work. Evaluation of the total uncertainty is performed in three steps: (1) The probability density function (PDF) of the cost function is obtained from simulated synthetic signals with model-surface-atmosphere noise without $\mathbf{S}_{\mathbf{e,CH}}$ and various cloud properties that follows the climatological distribution in the TEST week and is used as the "Benchmark" PDF of the cost function, (2) $\mathbf{S}_{\mathbf{e,CH}}$ is parameterized with six coefficients , and (3) we obtain the best combination of the parameters that exhibits the most similar PDF of the cost function to the Benchmark PDF from measurements over the TEST week based on the Monte Carlo method. The schematic diagram of this analysis is shown in Figure 2.

The noise-synthetic measurement signals are computed by the forward model calculations for a perturbed atmosphere-surface state and various cloud properties. The climatological distribution of cloud properties in the TEST week are obtained from optimal retrievals without considering $\mathbf{S}_{\mathbf{e,CH}}$ which is a function of COT. About half of the pixels in this week produce optimal solutions. Random noises of the atmospheric and surface states obey the error covariance matrices for each state. The Benchmark PDF of the cost function is evaluated based on the simulations from the synthetic noise and the true uncertainty ($\mathbf{S}_{\mathbf{e,w/oCH}} = \mathbf{S}_{\mathbf{e}} - \mathbf{S}_{\mathbf{e,CH}}$). This PDF idealizes and assumes that the error estimation is perfect, but measurement signals contain uncertainty due to cloud heterogeneity in addition to $\mathbf{S}_{\mathbf{e,w/oCH}}$. The PDF of the cost function based on the TEST week is compared with the Benchmark PDF by

$$\chi^2 = (\Delta\text{Mean})^2 + (\Delta\text{Stddev})^2 + (\Delta\text{Skew})^2, \tag{9}$$

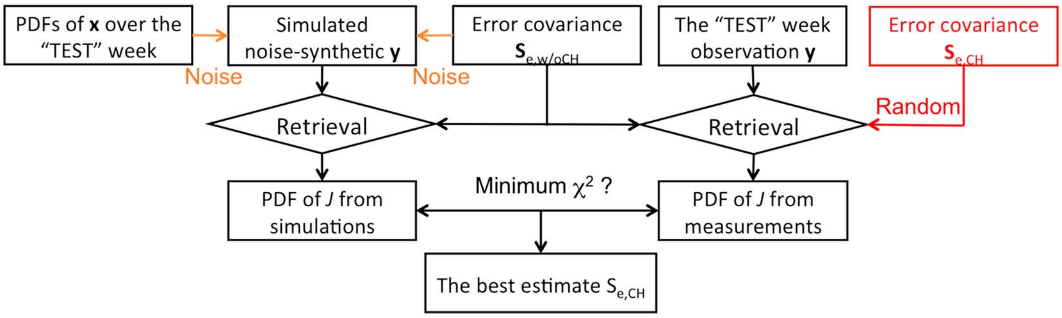

Figure 2. A schematic diagram of the analysis to evaluate an error covariance matrix in cloud heterogeneity.

where ΔMean, ΔStddev and ΔSkew are the average, standard deviation, and skewness difference between the Benchmark PDF and the PDF from the TEST week. The original PDF of the cost function is substantially skewed. Therefore, this study uses the logarithm of the cost function (ln *J*).

Figure 3 illustrates the PDF of the logarithm of the cost function obtained from simulations and observations.

The analysis is limited over the tropics due to computational burden. When the noise in the simulated synthetic measurements increases, the mean logarithm cost function of the retrieval also becomes large due to underestimation of the error covariance matrix as shown in the noise-enhanced cases (multiplied by a factor of 2 and 5). With retrievals from observations without $\mathbf{S}_{e,CH}$, the PDF has a broad width and a mean value larger than the ideal case. Using the best estimate of $\mathbf{S}_{e,CH}$, the retrievals have a mean value comparable to the ideal case, but the PDF has an unacceptably large width. Several possible sources cause substantial dispersion in the PDF of the logarithm of the cost function. One source is aerosols with variable optical properties in TIR radiation. The absorption properties of mineral dust show quite different spectral dependence in comparison with the counterpart in the case of ice crystals. This potentially affects BT by several kelvin in the split-window bands [*Ackerman*, 1997]. Another uncertainty is undetected liquid phase clouds. The CALIOP foot print is much smaller than the 1×1 km pixel size of IIR measurements. Therefore, IIR measurements are potentially affected by liquid low clouds even if the CALIOP lidar does not detect it. Those two sources are not considered in the current simulations but lead to significant biases of TIR BT. Moreover, magnitude of cloud heterogeneity might significantly vary, and this possibly enlarges the PDF width. Further investigations and rigorous evaluations in those error sources are needed and are left for future work. The simulations cannot explain these biases, and therefore, the retrieval cost function is larger. However, the PDF width does not change over simulations with several noise magnitudes and retrievals with/without $\mathbf{S}_{e,CH}$. This implies that this noise error does not affect the PDF width very much. The estimated RMSE of signals associated with cloud heterogeneity is about 0.5 (2.0) K for each TIR band when COT is 0.1 (1), which is comparable to results from *Fauchez et al.* [2014]. For this reason, this study uses the estimated $\mathbf{S}_{e,CH}$ as the uncertainty due to cloud heterogeneity at this moment. Note that this error covariance matrix may contain other uncertainties in cloud properties (e.g., ice crystal habit and surface roughness), and the TIR simulation does not consider those variability sources.

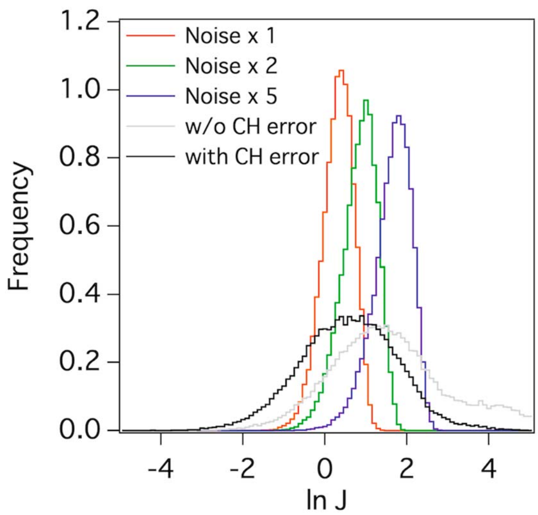

Figure 3. Probability density function of the logarithm of the cost function (ln *J*). CH indicates cloud heterogeneity.

4. Results and Discussions

4.1. Retrieval Error Analysis

The performance of the present retrieval algorithm is evaluated with synthetic noise signals [*Iwabuchi et al.*, 2014]. Synthetic measurement signals under various atmosphere-cloud conditions are simulated, and 1000 retrieval simulations from the signals are performed for each combination of cloud property state. Finally, the

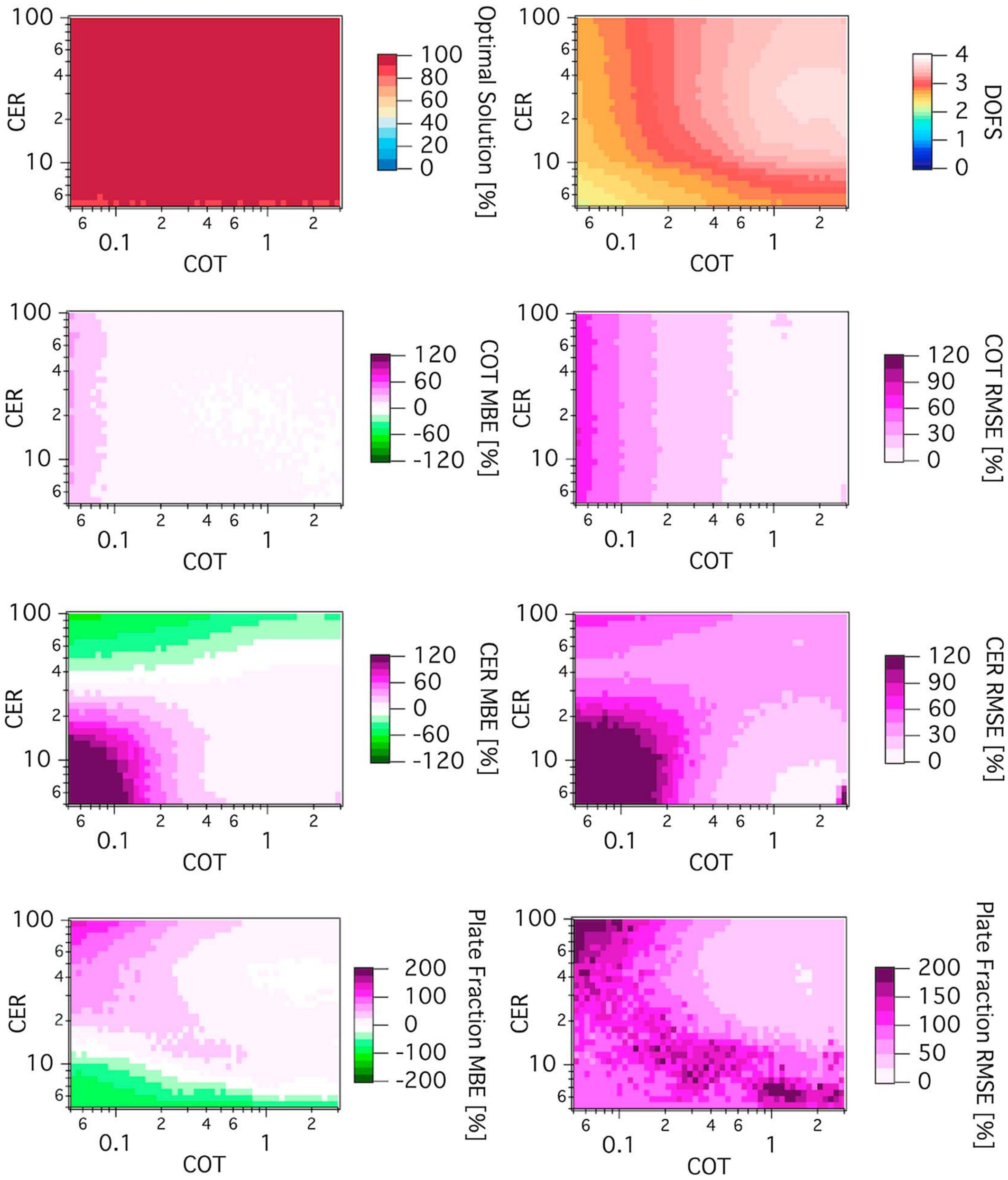

Figure 4. Simulated retrieval performance over ocean in the tropics. The mean bias errors (MBEs) and the root-mean-square errors (RMSEs) for COT, CER, and the plate fraction for each combination of COT and CER are evaluated. In addition, the fraction of optimal solutions and the degree of freedom for signal (DOFS) in each COT−CER condition are shown. The initial value of the plate fraction is 0.05% and surface roughness is 0.5 (severely roughened). The results assume CTH (cloud top pressure; CTP) of 12 km (213 hPa) and SST of 300 K.

mean bias errors (MBEs) and the RMSEs of the retrievals are evaluated by comparing retrieved cloud properties with the initial states of the properties. The model atmosphere is assumed to be tropical with a SST of 300 K. The corresponding CTH and CBH are fixed at 12 and 10 km, respectively.

Figure 4 shows the results of retrieval performance tests.

The tests are performed for various combinations of COT and CER from 0.03 to 3 and from 5 to 100 μm with plate fraction 0.05% and surface roughness 0.5 (severely roughened). The fraction of optimal solutions, the degrees of freedom for signals (DOFS) and MBEs and RMSEs for COT, CER, and plate fraction are evaluated from the case that produces an optimal solution ($J \leq 10$). Over this range of COT and CER, the retrieval method obtains optimal solutions in more than 90% of the simulations. The DOFS is greater than 3.5 when COT and

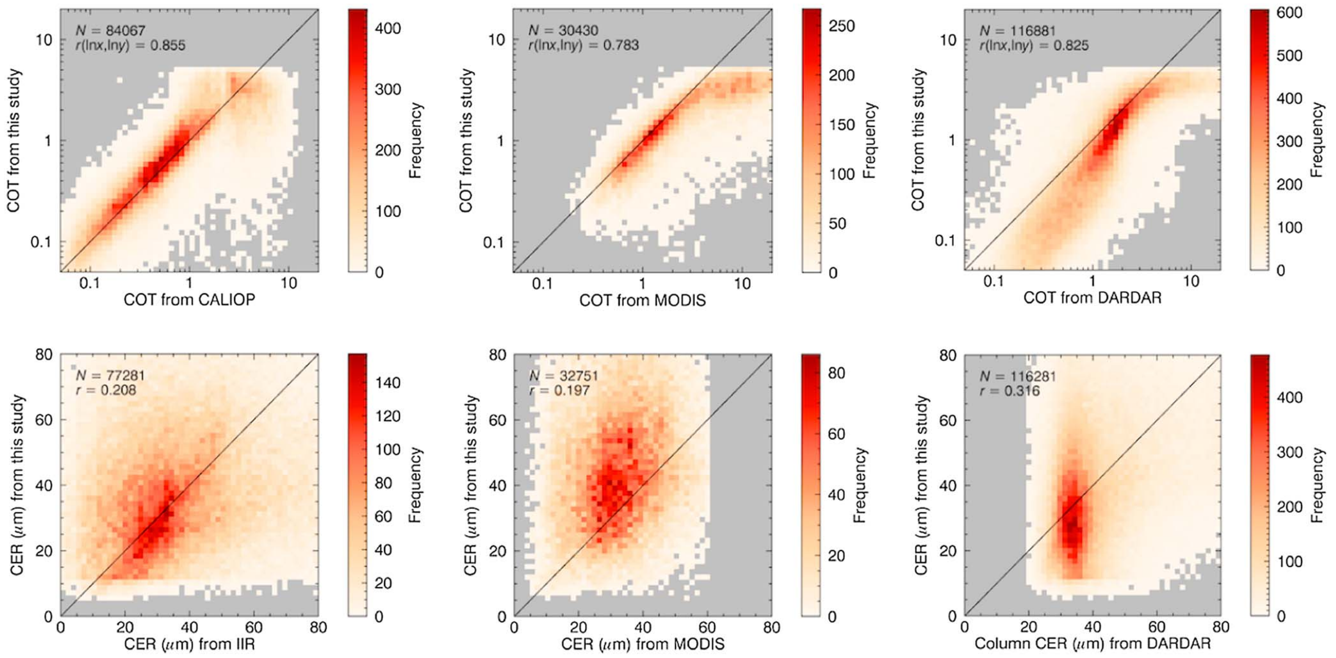

Figure 5. Two-dimensional histograms of COT and CER based on pixel-by-pixel comparisons between the present results and CALIPSO (left column), MODIS (middle column), and DARDAR products (right column) in the week from 1 to 7 April 2007.

CER are > 0.3 and > 10 μm and reaches 3 even if the COT is around 0.1. The COT MBEs are within $\pm 10\%$ over the prescribed range even where COT < 0.1. The RMSEs of COT retrievals are quite small, below 30% for COT of 0.3 or more and 50% at COT < 0.1. This is because the lidar signals provide information about thin clouds and TIR signals have substantial information content about thicker clouds. The CER retrievals have estimated MBE and RMSE of $\pm 20\%$ and $< 45\%$ under the conditions with COT > 0.3. For COT less than 0.3, the signals have little sensitivity to CER, seen in sensitivity tests with the TIR forward model, and consequently, the retrieved CER becomes close to the a priori. For the plate fraction, the MBE is within $\pm 20\%$ for COT greater than 0.3 and the RMSE is below 100% for COT and CER > 0.3 and > 10 μm, respectively. The RMSE is below 50% for COT greater than 0.5 and CER greater than 20 μm. Therefore, the tests demonstrate that this retrieval method is suitable for investigating cirrus clouds. The MBEs of the surface roughness reach $\pm 200\%$ over most of the region except for clouds with plate fraction less than 0.03% (not shown). This is because the sensitivity of the lidar signals to surface roughness becomes weak with increasing plate fraction, and the signal sensitivity is barely above the noise level. When the plate fraction is less than 0.03%, the results show that the MBE and RMSE of the surface roughness are from -50% to -80% and $\sim 100\%$ with surface roughness greater than 0.1.

4.2. Validation

To confirm the performance of the algorithm, several validation experiments are performed with the CALIOP L2 CLay 1 km and 5 km products, IIR L2 Track cloud products, MODIS Collection 6 (C6) cloud products [*Platnick et al.*, 2017], and DARDAR version 2.1.1 cloud products [*Delanoë and Hogan*, 2010]. The spatial resolution of CALIOP profiles is adjusted to 1 km. The CALIOP-collocated pixels of those products are selected for the comparison. The DARDAR product has vertical profiles of CER, so we calculate the column CER from the profiles by the following equation.

$$r_{\mathrm{eff,column}} = \frac{3}{4}\frac{\int_0^\infty V\mathrm{d}z}{\int_0^\infty A\mathrm{d}z} \tag{10}$$

$$= \frac{\int_0^\infty \mathrm{IWC}\,(z)\mathrm{d}z}{\int_0^\infty \frac{\mathrm{IWC}\,(z)}{r_{\mathrm{eff}}(z)}\mathrm{d}z}, \tag{11}$$

where A, V, and IWC are particle projected area, volume, and ice water content, respectively. The comparisons are performed with both daytime and nighttime retrievals over ocean.

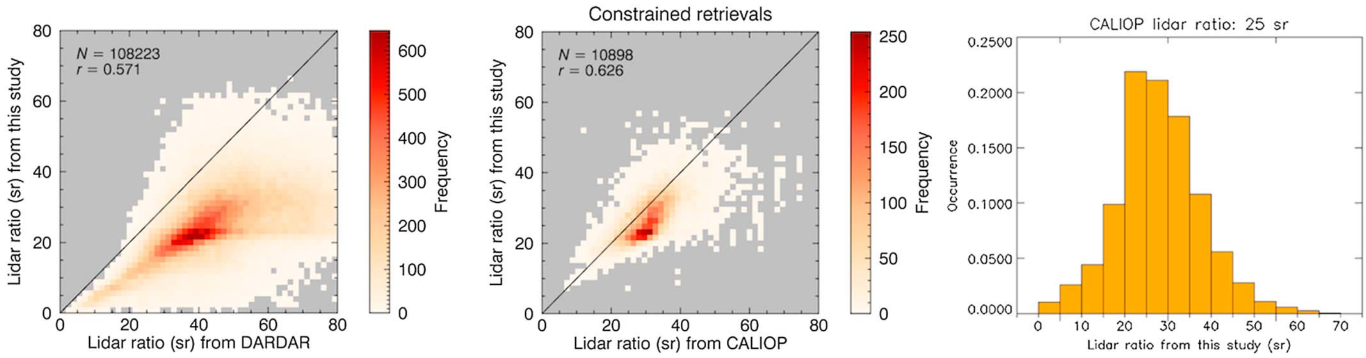

Figure 6. The lidar ratio comparisons obtained from this study and the DARDAR products (left), CALIOP constrained retrievals (middle), and CALIOP unconstrained retrievals with the initial lidar ratio of 25 sr (right), respectively.

COT and CER are first compared with these satellite products over a week (1 – 7 April 2007) on a pixel-by-pixel basis. Figure 5 shows COT and CER comparisons among those products when COT ranges from 0.05 to 5 and CER ranges from 0 to 80 μm.

Note that the comparison with MODIS C6 products are limited to daytime observations. COTs from this study are consistent with those CALIOP products and MODIS C6 products with correlation coefficients of 0.855 and 0.783, respectively. The MODIS C6 product misses pixels when COT is less than 0.3, and the number of pixels available for comparison is about a quarter of the CALIOP products, which implies that MODIS misses about half of the cloud over this range. This study underestimates COTs where COT obtained from MODIS or DARDAR is larger than 5. Possible reasons are that (1) lidar and TIR measurements are less sensitive to such large COT than shortwave and radar measurements and (2) CALIOP measurements may miss some clouds that are detected by MODIS and radar due to smaller footprints of CALIOP measurements than those of MODIS and radar. COTs of DARDAR products are substantially higher compared with this study, especially in optically thin cloud. Figure 6 compares the lidar ratio (S) among the present results, the DARDAR products and the CALIOP L2 CLay 5 km product based on the constrained and unconstrained retrieval methods [*Young and Vaughan*, 2009]. In this study, the lidar ratio is calculated from the bulk optical properties based on the inferred parameters. The results demonstrate that the lidar ratios from DARDAR products are about twice as large as those from this study.

This bias causes the COT bias in DARDAR products. In contrast, the lidar ratios from this study generally agree with but slightly lower than those from the CALIOP constrained retrievals, showing correlation coefficient of 0.626. It would be desirable to understand how the lidar ratio retrieved from this study is distributed over the pixels where the initial lidar ratio (25 sr) is used in the CALIOP. For COT inferences over transparent cirrus clouds, 99.7% of the CALIOP unconstrained retrievals use the initial lidar ratio of 25 sr. The distribution of lidar ratio from this study exhibits a peak at ~25 sr, but large dispersion ranged from 2 to 65 sr. This implies that use of a constant lidar ratio as an initial value over the globe is not a sufficient approach for COT inference from the CALIOP measurements with the unconstrained retrieval method. CER retrievals show low consistency between this study and other products with correlation coefficients from 0.2 to 0.3, but the mean values agree well with IIR and DARDAR products.

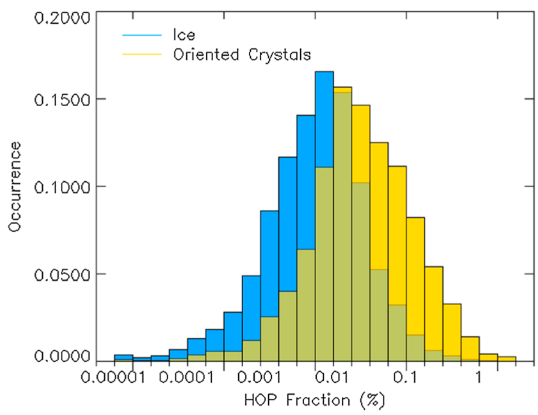

Figure 7. Histograms of the HOP fraction retrieved from this study. Blue and yellow colors are from the pixels corresponding to ice and oriented ice crystals diagnosed by the CALIOP over the week from 1 to 7 April 2007.

The HOP fraction is compared with the detections of oriented ice crystals by the CALIOP over the week. Figure 7 shows the histograms of HOP fraction for each CALIOP cloud phase diagnosis.

The HOP fraction is generally higher in the oriented ice crystals pixels than the ice pixels, and median values of the HOP fraction is 0.024%

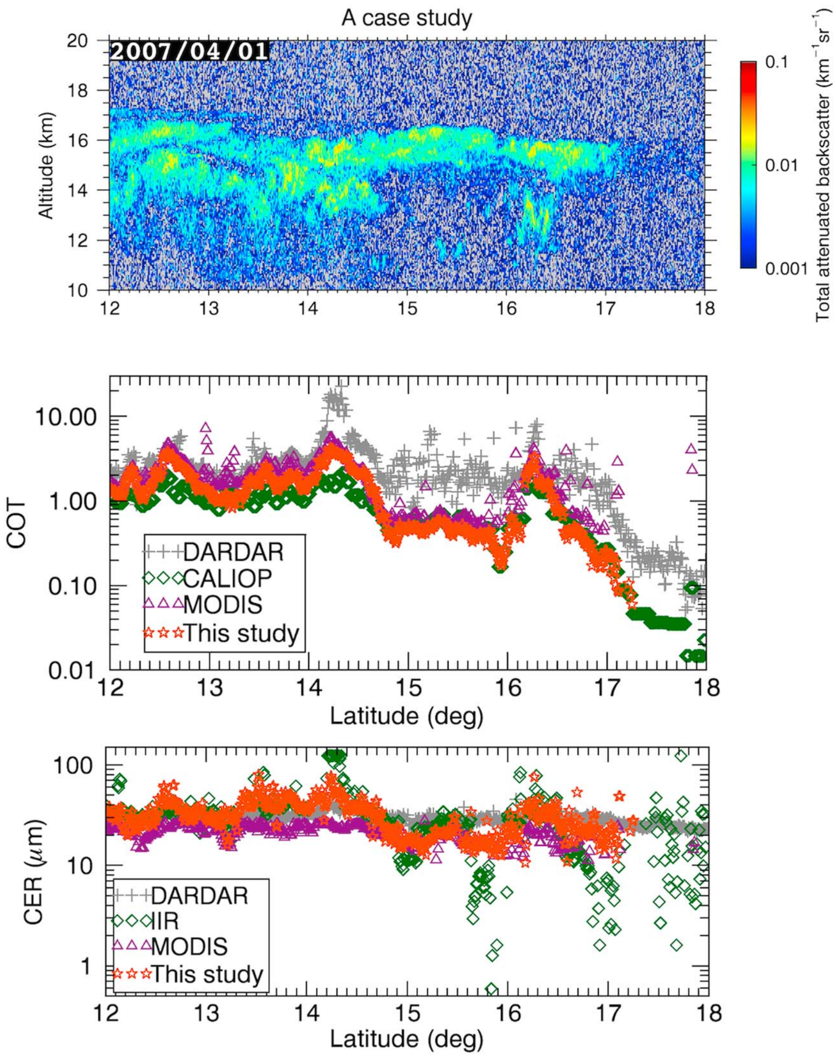

Figure 8. A case study over the west Pacific Ocean ranged from 12°N–18°N on 1 April 2007. Intercomparison among this study, MODIS, CALIPSO and DARDAR products are performed. The upper panel shows the total attenuated backscatter from the CALIOP level-1b products. The middle and bottom panels show COT and CER for each product.

and 0.0064% over the oriented ice crystals and ice pixels, respectively. Therefore, the HOP fractions from this study essentially agree with detections of oriented ice crystals by the CALIOP. A part of both histograms is overlapped around the HOP fraction of ∼ 0.01%. This could be principally caused by the algorithm differences between the present method and CALIOP feature classification [*Hu et al.*, 2009]. This study considers CER and the degree of surface roughness for lidar signal calculations but does not take into account spatial coherence in lidar signals, unlike in the CALIOP feature classification.

Next, these products are compared in the West Pacific tropics from 12°N to 18°N in latitude and at longitude 168°E as a case study. Figure 8 shows vertical profiles of the total attenuated backscatter from CALIOP level 1b products and the pixel-by-pixel comparison of COT and CER over the granule.

Optically very thin cirrus cloud is spread over the range of 17°N–18°N and is gradually becoming optically thick toward the south, but the cirrus clouds are transparent. Note that there are possible multilayer clouds (such as at latitudes 16°N–16.5°N), but the retrieval analysis is performed as a single-layer cloud based on the criteria described above. The COT retrievals of this study are consistent with CALIOP cloud products when COT is 1.0 or less and are close to MODIS C6 products when the COT is thicker. A systematic bias in the COT comparison between this study and DARDAR cloud products is found over clouds with COT < 1. The CER retrievals of this study generally agree with IIR products but do not exhibit the large dispersion shown by IIR CERs over the region. Comparisons with the MODIS C6 product do not show good agreement for a cloud with

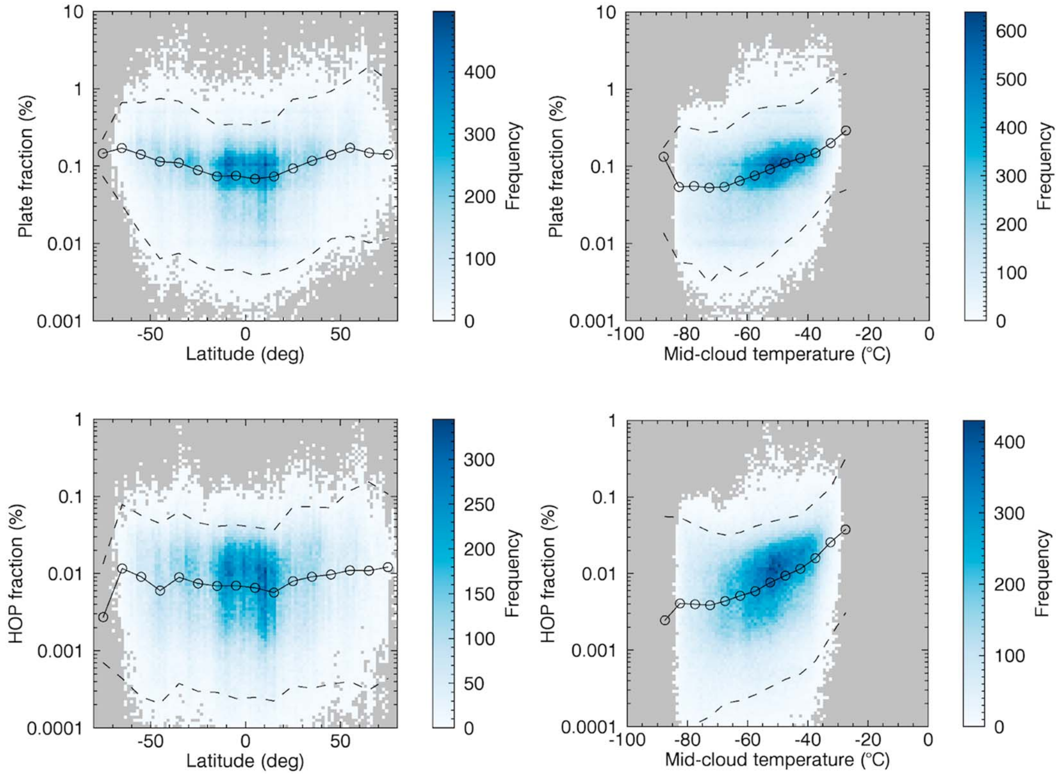

Figure 9. Global analysis for April 2007 focusing on the plate fraction and HOP fraction. Right and left columns show the middle-cloud temperature and latitudinal variation of those properties, respectively. The solid line with circle symbols indicates the median value and the dashed lines show the 2.5 to 97.5% range.

COT greater than 1.0, showing an average CER $\sim$ 20 μm from MODIS and 30–40 μm from this study. This is partly because cloud vertical heterogeneity provides different impacts on CER retrievals between MODIS and this study in moderately optically thick clouds [*Zhang et al.*, 2010]. The CER from DARDAR product shows low variability with an average of 25 μm over the region.

Based on the above, the present method is suitable for investigation of cirrus clouds and is applicable for clouds with a wide COT range from 0.03 to 3, over which accuracy of retrievals is acceptable.

4.3. Global Statistics of Plate Particles

Using data from April 2007, in which the CALIOP off-nadir angle is 0.3°, this algorithm focuses on ice particle morphology. In this study, cirrus clouds are defined by COT less than 3, cloud top temperature (CTT) less than −40°C, and geometrical thickness less than 3 km, according to criteria and findings in *Sassen et al.* [2008]. First, the algorithm is processed for the pixels that satisfy the requirements shown in Table 2. Second, we choose pixels that satisfy the criteria for cirrus clouds as shown above. Finally, to guarantee the accuracy of cloud property retrievals, pixels with optimal solutions, CER of 5–80 μm and DOFS greater than 3 are selected. As a result, 90% of cirrus pixels ($N = 341162$) are used in the following analysis.

Figure 9 shows latitudinal and temperature variations of the plate fraction and HOP fraction in cirrus clouds.

The median COT is 0.2 in the tropics (30°S–30°N), 0.3 in midlatitudes (30°S–60°S and 30°N–60°N), and 0.5 in high latitudes (> 60°S and > 60°N). Generally, the distributions of those properties exhibit large variabilities of 2 orders of magnitude. The plate fraction shows latitudinal variation with a median of 0.06% in the tropics and 0.1% at higher latitudes. The middle-cloud temperature (MCT) is defined as the average temperature of the cloud top and base in this study. The distribution of the plate fraction exhibits significant dependence on the MCT, with median 0.04% at MCT of −80°C and 0.1% at MCT of −40°C. The HOP fraction shows the same tendency of variation in latitude and MCT, but the fraction is generally one-tenth of the plate fraction. Since CERs range from 15 to 50 μm with a median of 32 μm in this analysis, generally, cirrus clouds consist of small particles and do not contain many large particles (>100 μm) where HOPs can exist. In consequence, the HOP

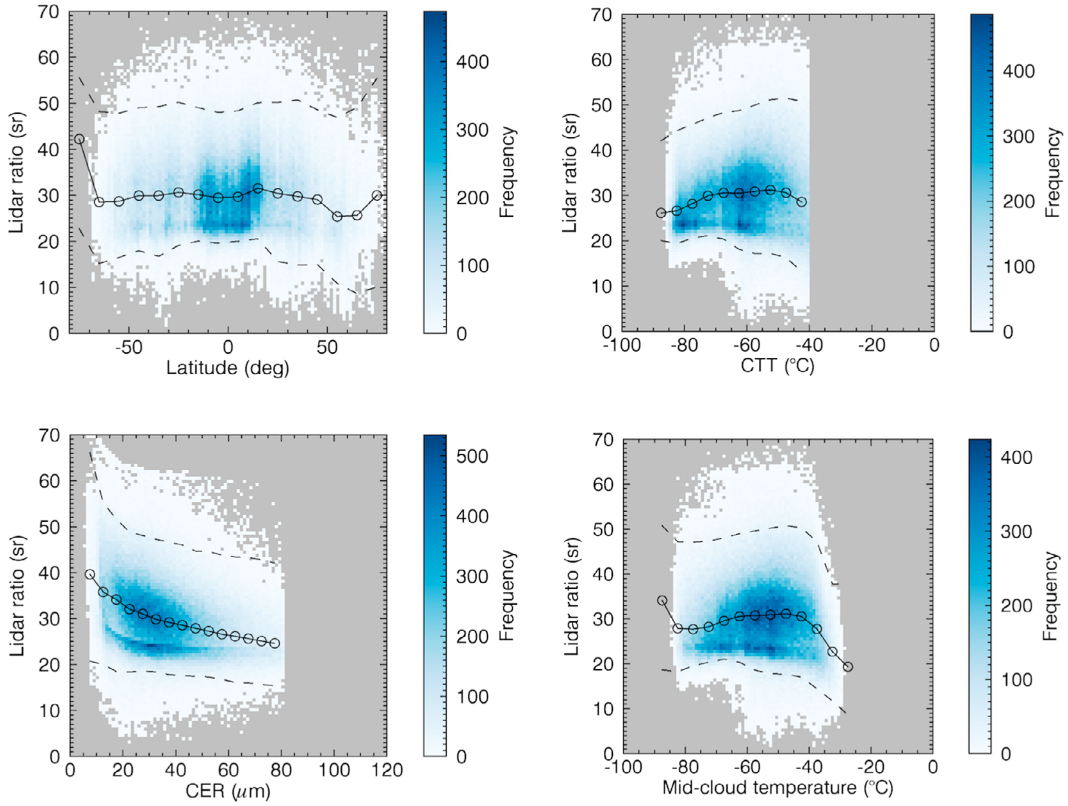

Figure 10. Distributions of the lidar ratio with respect to the cloud top temperature (CTT), the middle-cloud temperature, cloud effective radius (CER), and latitude. The solid line with circle symbols indicates the median value and the dashed line show the 2.5 to 97.5% range.

fraction is ~ 0.01%, which is significantly smaller than measured by previous studies [*Noel and Chepfer*, 2004, 2010]. Several papers have reported that surface texture of ice crystals may not be perfectly smooth [*Magee et al.*, 2014], although a smooth surface is assumed in the hexagonal plates in this study due to limitation of PGOH computation. HOPs with a roughened surface may provide weaker backscattering intensity and higher depolarization ratio than those with a smooth surface, and therefore, this study could underestimate the plate and HOP fraction if clouds contain roughened plate particles.

Figure 10 shows distributions of the lidar ratio variation in cirrus clouds.

Those distributions exhibit large variability as well. The median lidar ratio of cirrus cloud over the globe is about 27–31 sr, which generally agrees with *Seifert et al.* [2007] with a mean lidar ratio of 29–33 sr over the Indian Ocean and with *Josset et al.* [2012] with a lidar ratio of 33 ± 5 sr over the global ocean. In addition, slight latitudinal variations with higher values in the tropics and lower value in high latitude are seen. With increasing CERs, the lidar ratio decreases due to increase of HOPs. A distribution of the lidar ratio with respect to CTT exhibits weak dependence on temperature where the CTT is less than −40°C but takes a slightly lower value in colder temperatures (< −60°C) and shows larger dispersion over warmer CTTs. Similar results for cold cirrus clouds are also found in *Garnier et al.* [2015], implying that less complex ice crystals are dominant at colder temperature. The slight temperature dependence of lidar ratio could also be explained with the degree of surface roughness of ice crystals that will be discussed in section 4.4. The lidar ratio sharply decreases where MCT is higher than −40°C when the HOP fraction reaches 0.01%. The temperature of −40°C is a critical point in terms of the lidar ratio, since a HOP fraction greater than 0.01% has substantial effect on the IAB.

Lidar measurements detect geometrically thick transparent ice clouds that satisfy the same criteria as cirrus clouds (COT less than 3 and CTT less than −40°C) but with cloud geometric thickness greater than 3 km. After quality control filtering, the number of cases reaches $N = 141,299$. Figure 11 shows the distribution of the HOP fraction and the lidar ratios for transparent thick clouds.

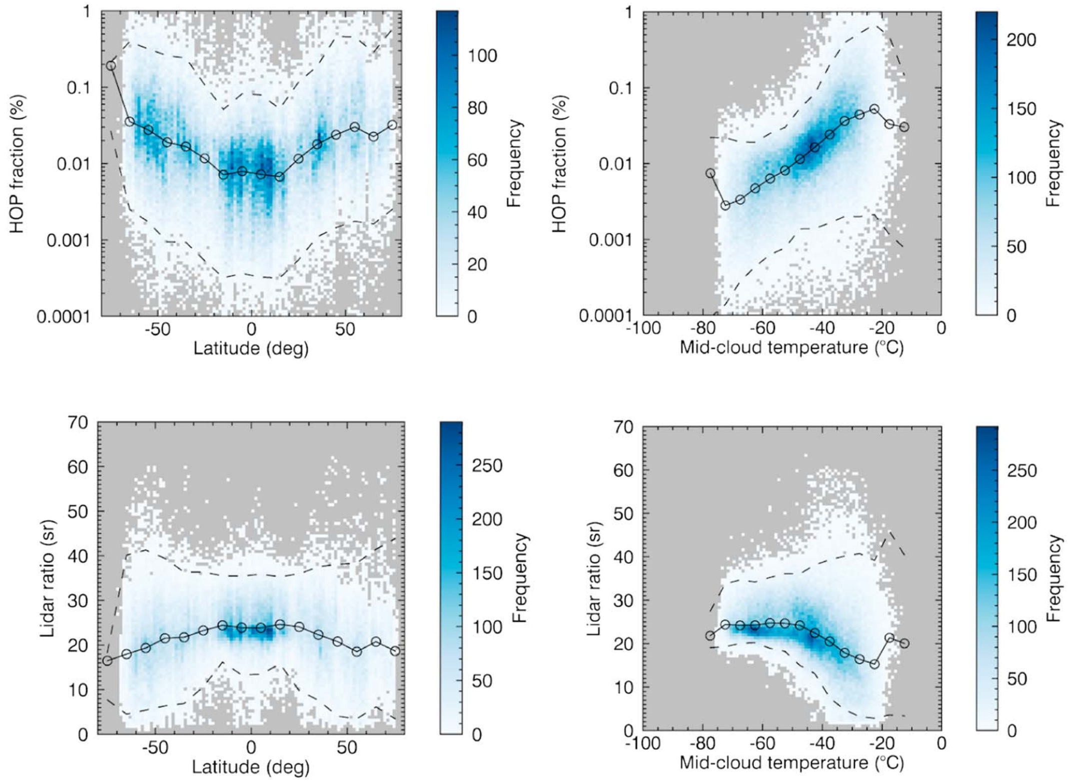

Figure 11. The distribution of the HOP fraction (top row) and lidar ratio (bottom row) for transparent ice clouds with CTT of −40°C, COT of 3 or less but cloud geometric thickness larger than 3 km. Left and right columns show the latitudinal variation and middle-cloud temperature dependence of those properties, respectively. The solid line with circle symbols indicates the median value and the dashed lines show the 2.5 to 97.5% range.

The median COT is 1 in the tropics and 2 in high latitudes, which is optically thicker than for cirrus clouds with geometric thickness less than 3 km, as shown by *Sassen and Comstock* [2001]. The median HOP fraction is 0.003%, 0.009%, and 0.04% at MCTs of −70°C, −50°C, and −30°C, respectively. As several previous studies indicate [e.g., *Noel and Chepfer*, 2010], the temperature where HOPs are frequently present is greater than −30°C, and therefore, the lidar distributions exhibit substantial latitudinal variation. Figure 12 shows the COT comparison between this study and the CALIOP. The results exhibit high correlation coefficients in the tropics (0.909) and extratropics (0.903) in case of comparison with the CALIOP constrained retrievals. The comparison with the CALIOP unconstrained retrievals also shows good agreement in the tropics with a correlation coefficient of 0.761 because the median lidar ratio in the tropics is close to 25 sr with relatively small dispersion. However, the ratio in the extratropics (latitude greater than 30°) provides a negative bias, where COT is greater than 1 and a relatively low correlation coefficient of 0.614. This is because the lidar ratio over the extratropics has large dispersion, and the median value is lower than 20 sr, which is far from the initial value used in the CALIOP products. The results suggest that more precise initial lidar ratio, which may be a simple temperature-based parameterization of the lidar ratio, could significantly improve CALIOP COT retrievals with the unconstrained retrieval method.

4.4. Discussions of Ice Particle Morphology

This study shows quantitative distributions of the fraction of plates and HOPs. However, several assumptions have impacts on quantitative retrievals. The assumption of the tilting angle of HOP is critical since a small tilting angle (< 1°) dramatically intensifies the backscattering. There is a general consensus that the tilting angle of HOP is usually less than a few degrees [*Sassen*, 1991; *Sassen and Benson*, 2001; *Reichardt et al.*, 2002]. This study investigates the impacts of the tilting angle assumption on the retrievals.

Figure 13 shows histograms of the plate fraction and lidar ratio inferred from this study by assuming a mean tilting angle of 0.8°, 0.9°, and 1°, respectively.

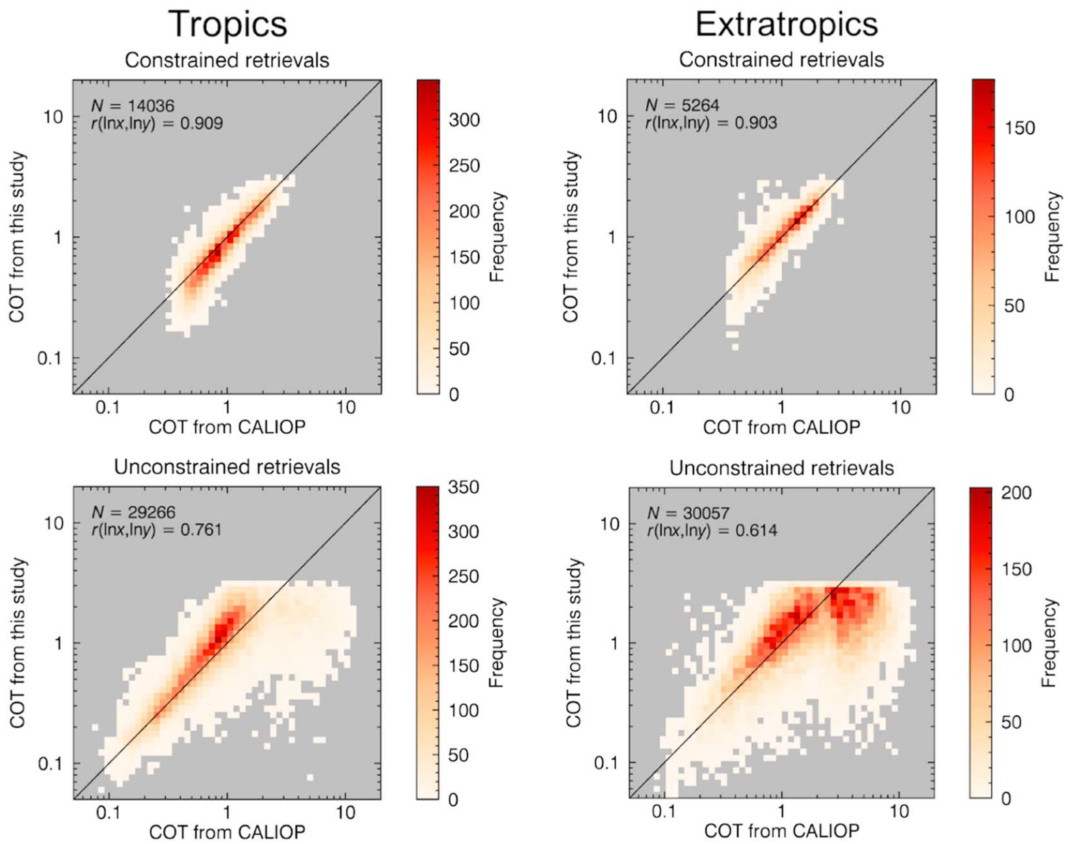

Figure 12. Pixel-by-pixel comparison of COT from this study with the CALIOP constrained retrievals (top row) and unconstrained retrievals (bottom row) for transparent ice clouds with CTT of −40°C, COT of 3 or less but cloud geometric thickness larger than 3 km. Left and right columns exhibit the comparison with the CALIOP products over the tropics and extratropics.

The plate fraction shifts to a larger value when the average tilting angle increases. However, general feature assumptions of the plate fraction such as latitudinal variation and temperature dependence are not changed when solving for the plate fraction and lidar ratio. Note that the probability density of the lidar ratio is almost identical over the tested tilting angles and the distribution exhibits the same characteristics as shown in Figure 10. Other retrievals such as COT, CER, and the degree of surface roughness are not affected much as well, and those averages vary less than 1% among the three cases. The average value of the plate fraction varies within a factor of 3, but that is smaller than the magnitude of variability of the plate fraction with respect to

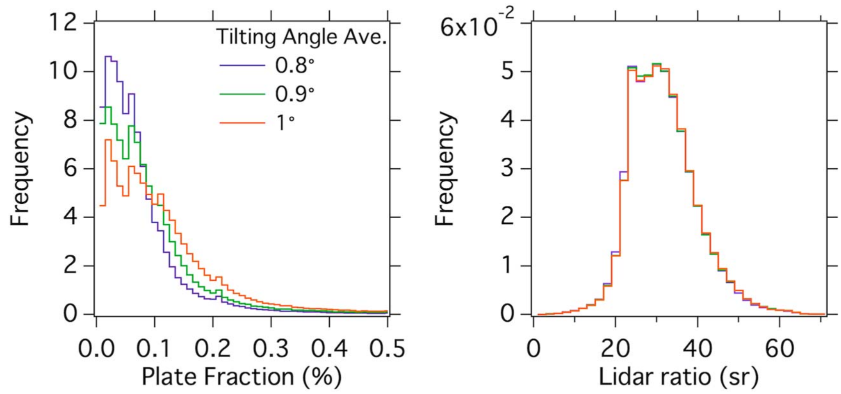

Figure 13. The histogram of the plate fraction and lidar ratio in cirrus clouds for each assumed tilting angle PDF.

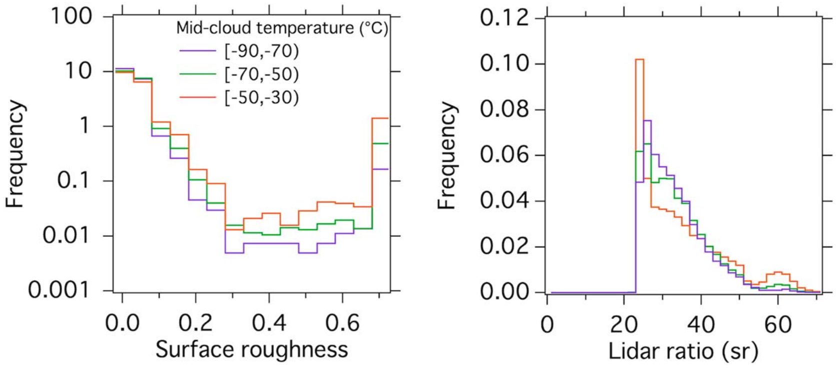

Figure 14. The histogram of the retrieved surface roughness and lidar ratio in cirrus clouds with a plate fraction less than 0.03%.

temperature. Thus, the latitudinal variation and temperature dependence of the plate fraction as well as the lidar ratio are robust features, even if the quantitative value of the plate fraction is uncertain in some cases.

The other assumption is the use of the column aggregate particle model for complex ice particle morphologies. In fact, cirrus clouds consist of a variety of ice particle shapes with significant temperature dependence. In a cloud temperature less than −50°C, the cirrus cloud consists mostly of small droxtals (also known as compact facets) [*Heymsfield and Iaquinta*, 2000; *Lawson et al.*, 2006]. Plate aggregate particles (bullet rosette particles) generally increase where temperature is less (greater) than −40°C [*Bailey and Hallett*, 2009]. *Iwabuchi et al.* [2012] investigated backscattering properties of various ice particle shapes to aim for better understanding of particle texture in contrails. The optical properties of different ice crystals such as droxtals, hollow columns, bullet rosettes, and column aggregates vary within a range of 0.1 for the depolarization ratio but by a factor of 3 or more for the lidar ratio when each particle has a smooth surface. Variability due to different particle shapes is almost the same magnitude as variability with changes in the surface roughness, as shown in Figure 1c, but may not have significant impacts on the retrievals of the plate fraction in terms of a sensitivity magnitude.

Retrieval of the degree of surface roughness is also investigated under very limited cloud conditions. We chose cirrus clouds with a plate fraction less than 0.03%, and 18.05% of the cirrus pixels ($N = 61576$) are analyzed.

Figure 14 shows temperature dependence of the degree of surface roughness and the lidar ratio in this study. As discussed above, the inferred surface roughness may represent not only the surface roughness itself but also complexity of the crystal shape. The distribution is bimodal with peaks at both limits of the prescribed range, implying that the prescribed range may not be large enough. A majority of pixels indicates that aggregates have smooth surface roughness that is not consistent with previous studies [*van Diedenhoven et al.*, 2014; *Hioki et al.*, 2016]. One of the possible reasons is that the column aggregate model may not be suitable for cirrus clouds, which is discussed above. The other possible reason is that the backscattering intensity at a scattering angle of ~ 180° is underestimated with current computing techniques, even including the backscattering correction. Further constraints of the ice particle shape model and improvements of computational techniques for light scattering properties are needed. The distribution of the degree of surface roughness exhibits a slight dependence on temperature, indicating that more roughened particles are present where the MCT is warmer. In the three bins discriminated by the MCT, the average CER values are 34.1 μm, 38.2 μm, and 41.8 μm for MCT ranged from −90°C to −70°C, −70°C to −50°C, and −50°C to −30°C, respectively. The lidar ratio distribution differs among those bins, resulting mainly from variation in CERs for a small lidar ratio and variation of roughened particles ($\sigma^2_{POLY} > 0.1$) for a large lidar ratio. A small peak at the lidar ratio of ~ 60 sr corresponds to the presence of severely roughened particles. An absence of lidar ratios less than 25 sr is mainly caused by ice particles in clouds where HOPs are not present. Such clouds have significant variability in the backscattering intensity, causing large dispersion of the lidar ratio. Significant temperature dependence of ice particle morphology is shown in this study, but results still exhibit a large dispersion. Another important factor for ice particle morphology is ice supersaturation [*Bailey and Hallett*, 2004], which may contribute to the dispersion.

5. Conclusions and Future Prospects

We have developed an optimal estimation-based algorithm to infer ice particle morphology and microphysical properties in cirrus clouds from measurements of thermal infrared radiances and lidar backscatter signals on the CALIPSO platform. The bulk optical properties take into account the HOPs and the column aggregates with various degree of surface roughness. Retrieval performance tests show that the method can infer not only COT and CER but also the plate fraction without significant biases and demonstrate that this technique is suitable for investigation of COT (CER and the plate fraction) in cirrus clouds with a lower COT limit of 0.03 (0.3). Validation tests with other satellite-derived products show that COT retrievals are consistent with CALIOP and MODIS products. Inconsistency in COT compared with DARDAR products results from a discrepancy in the lidar ratio, which is retrieved simultaneously from both products: The ratio from DARDAR products is about twice as high as the one from this study. Comparisons of CERs show large discrepancies and low correlation coefficients among the products. An analysis of 1 month of data shows distributions of the fraction of plate particles and HOPs (April 2007). Those properties have substantial dependence on temperature, resulting in their latitudinal variations. The HOP fraction is about 0.003% at a middle-cloud temperature of −80°C and 0.01% at MCT of −40°C. Those quantities may be uncertain due to uncertainty in the average tilting angle, but the temperature dependence of plates and HOP is robust. The lidar ratio theoretically calculated from inferred optical properties in cirrus is 27–31 sr, which is consistent with previous studies, and the value is smaller at high latitudes, compared to the tropical counterpart. Cirrus clouds with a geometrically thick structure exhibit large variability in the lidar ratio over the extratropics, resulting in relatively worse correlation coefficients based on comparisons of COT with CALIOP products.

Use of measurements from multiple satellite instruments gives more precise retrievals, since the retrievals can explain those multiple signals. As shown by comparison between this study and other products, the same retrievals from different instruments frequently show discrepancies. Ultimately, the most precise retrievals explain all measurements. This study has the potential to improve the accuracy of retrievals and take into account more parameters for inferences by adding other measurement signals such as cloud reflectivity at visible and near-infrared wavelengths, radar reflectivity over clouds, and multiangle polarized cloud reflectivity. Additional data substantially increase the information content of cloud properties, including ice particle morphology, and gives us more precise understanding of cirrus cloud properties as well as cirrus cloud radiative effects.

This study demonstrates the statistics of ice particle morphology based on 1 month of global satellite data. The CALIPSO satellite has provided TIR and the lidar signals since it was launched in 2006, and more than 10 years of data are available. In addition, the Earth Clouds, Aerosol and Radiation Explorer (EarthCARE) satellite will be launched in 2018, and it has similar instruments compared to CALIPSO [*Illingworth et al.*, 2015]. The method in this study is applicable to future measurement signals from the EarthCARE satellite. Therefore, investigation of ice particle morphology in cirrus clouds over a multidecadal period shall be possible.

Appendix A: Backscattering Correction

The conventional geometric optics method is not capable of providing the accurate phase function values in backscattering directions since the method does not take interference into account, thereby underestimating backscattering. *Zhou and Yang* [2015] provided a method to correct the phase function over scattering angles of 175–180° for hexagonal column particles. The method uses the sinc function to represent a pattern of interference fringes that presumably happen due to the coherent phase interference of scattered field in the case of a simple particle morphology. However, a particle with a complex texture does not give rise to the same pattern according to a rigorously calculated phase function using the invariant-imbedding T matrix (II-TM) method [*Bi et al.*, 2013, 2014]. In this study, a backscattering correction at scattering angles near 180° is provided for the column aggregate shape particle based on the method from *Zhou and Yang* [2015] adjusted for complex particles. The amplification factor is described as $\xi(\theta) = \frac{P_{11,\mathrm{II-TM}}(\theta)}{P_{11,\mathrm{flat}}(\theta)}$, where $P_{11,\mathrm{II-TM}}(\theta)$ and $P_{11,\mathrm{flat}}(\theta)$ are the P_{11} values calculated from the II-TM and linear extrapolation from the scattering angle range of 150–175°. P_{11} in the scattering angle range of 175–180° is multiplied by ξ. For a continuous phase function at the angle of 175°, the correction factor ξ that should be multiplied by P_{11} is defined by

$$\xi(\theta) = F(\theta) - F(175^\circ), \tag{A1}$$

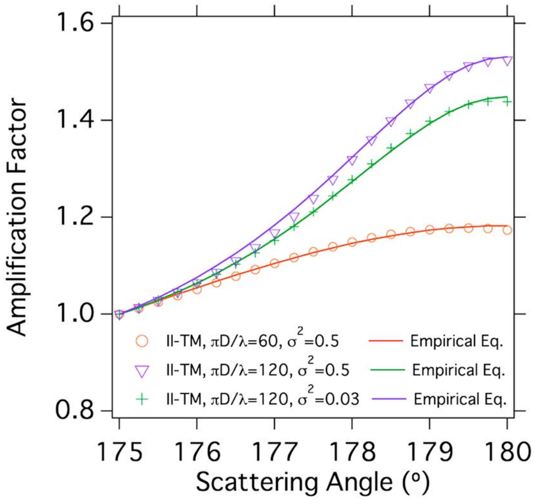

Figure A1. Scattering phase function (P_{11}) values of the column aggregate particle model obtained from the II-TM calculation (symbols) and the combined IGOM and a backscattering correction (lines) for specified combinations of size parameter and surface roughness.

where function $F(\theta)$ is the Cauchy distribution described as

$$F(\theta) = C_1 \frac{C_2^2}{(\pi - \frac{\pi\theta}{180})^2 + C_2^2}. \tag{A2}$$

Coefficients, C_1 and C_2 represent height and width of the backscattering peak. Based on a rigorous calculation with II-TM, C_1 is almost constant over the size parameter $\frac{\pi D}{\lambda}$ but takes a lower value for severely roughened particles compared to smooth particles, and C_2 does not depend on the surface roughness and is parameterized well for various size parameters as

$$C_2 = D_1 + D_2(\frac{\pi D}{\lambda})^{-D_3}, \tag{A3}$$

where D_1, D_2, and D_3 are coefficients that take positive values. Therefore, we determine those coefficients with least squares fitting to calculated phase functions using II-TM over the size parameter range of 40–130 µm and surface roughness range of 0.001–0.7.

Figure A1 shows amplification factors calculated from the II-TM (the exact values) and from the combined IGOM and backscattering correction.

The IGOM with the backscattering corrections constructs the backscattering peak of P_{11} over the scattering angle accurately.

Acknowledgments
The authors thank the Atmospheric Sciences Data Center for providing the CALIPSO products (https://eosweb.larc.nasa.gov/project/calipso/calipso_table), the NASA Earth Observing System Data and Information System for providing the MODIS data (https://earthdata.nasa.gov), and the Goddard Earth Sciences Data and Information Services Center for providing the MERRA data set (https://gmao.gsfc.nasa.gov/reanalysis/MERRA). The ice particle scattering calculations were conducted at the Texas A&M University Supercomputing Facility. The authors are grateful to Jiachen Ding for help in light scattering computations. This study was supported by Grant-in-Aid for Scientific Research (DC1 262947) and KAKENHI grant JP 25287117 from the Japan Society for the Promotion of Science (JSPS). The data provided by this paper are available from the first author upon request.

References

Akima, H. (1970), A new method of interpolation and smooth curve fitting based on local procedures, *J. Assoc. Comput. Mach.*, *17*(4), 589–602.

Ackerman, S. A. (1997), Remote sensing aerosols using satellite infrared observations, *J. Geophys. Res.*, *102*, 17,069–17,079.

Bailey, M., and J. Hallett (2004), Growth rates and habits of ice crystals between −20 and −70°C, *J. Atmos. Sci.*, *61*(5), 514–544.

Bailey, M. P., and J. Hallett (2009), A comprehensive habit diagram for atmospheric ice crystals: Confirmation from the laboratory, AIRS II, and other field studies, *J. Atmos. Sci.*, *66*(9), 2888–2899.

Baran, A. J., and L. C. Labonnote (2006), On the reflection and polarisation properties of ice cloud, *J. Quant. Spectrosc. Radiat. Transfer*, *100*(1), 41–54.

Bi, L., and P. Yang (2014), Accurate simulation of the optical properties of atmospheric ice crystals with invariant imbedding T-matrix method, *J. Quant. Spectrosc. Radiat. Transfer*, *138*, 17–35.

Bi, L., P. Yang, G. W. Kattawar, and R. Kahn (2010), Modeling optical properties of mineral aerosol particles by using nonsymmetric hexahedra, *Appl. Opt.*, *49*(3), 334–342.

Bi, L., P. Yang, G. W. Kattawar, Y. Hu, and B. A. Baum (2011), Scattering and absorption of light by ice particles: Solution by a new physical-geometric optics hybrid method, *J. Quant. Spectrosc. Radiat. Transfer*, *112*(9), 1492–1508.

Bi, L., P. Yang, G. W. Kattawar, and M. I. Mishchenko (2013), Efficient implementation of the invariant imbedding T-matrix method and the separation of variables method applied to large nonspherical inhomogeneous particles, *J. Quant. Spectrosc. Radiat. Transfer*, *116*, 169–183.

Borovoi, A. G., and I. A. Grishin (2003), Scattering matrices for large ice crystal particles, *J. Opt. Soc. Am. A*, *20*(11), 2071–2080.

Bréon, F.-M., and B. Dubrulle (2004), Horizontally oriented plates in clouds, *J. Atmos. Sci.*, *61*(1), 2888–2898.
Brown, O. B., P. J. Minnett, R. Evans, E. Kearns, K. Kilpatrick, A. Kumar, R. Sikorski, and A. Závody (1999), MODIS infrared sea surface temperature algorithm theoretical basis document version 2.0. University of Miami. [Available at: https://modis.gsfc.nasa.gov/data/dataprod/mod28.php.]
Chandrasekhar, S. (1960), *Radiative Transfer*, 393 pp., Dover, New York.
Chang, F.-L., and Z. Li (2005), A near-global climatology of single-layer and overlapped clouds and their optical properties retrieved from Terra/MODIS data using a new algorithm, *J. Clim.*, *18*(22), 4752–4771.
Cole, B., P. Yang, B. Baum, J. Riedi, and L. C-Labonnote (2014), Ice particle habit and surface roughness derived from PARASOL polarization measurements, *Atmos. Chem. Phys.*, *14*(7), 3739–3750.
Cole, B. H., P. Yang, B. A. Baum, J. Riedi, L. C. Labonnote, F. Thieuleux, and S. Platnick (2013), Comparison of PARASOL observations with polarized reflectances simulated using different ice habit mixtures, *J. Appl. Meteorol. Climatol.*, *52*(1), 186–196.
Cooper, S. J., and T. J. Garrett (2010), Identification of small ice cloud particles using passive radiometric observations, *J. Appl. Meteorol. Climatol.*, *49*(11), 2334–2347.
Cooper, S. J., T. S. L'Ecuyer, P. Gabriel, A. J. Baran, and G. L. Stephens (2006), Objective assessment of the information content of visible and infrared radiance measurements for cloud microphysical property retrievals over the global oceans. Part II: Ice clouds, *J. Appl. Meteorol. Climatol.*, *45*(1), 42–62.
Delanoë, J., and R. J. Hogan (2010), Combined CloudSat-CALIPSO-MODIS retrievals of the properties of ice clouds, *J. Geophys. Res.*, *115*, D00H29, doi:10.1029/2009JD012346.
Ding, J., P. Yang, R. E. Holz, S. Platnick, K. G. Meyer, M. A. Vaughan, Y. Hu, and M. D. King (2016), Ice cloud backscatter study and comparison with CALIPSO and MODIS satellite data, *Opt. Express*, *24*(1), 620–636.
Fauchez, T., C. Cornet, F. Szczap, P. Dubuisson, and T. Rosambert (2014), Impact of cirrus clouds heterogeneities on top-of-atmosphere thermal infrared radiation, *Atmos. Chem. Phys.*, *14*(11), 5599–5615.
Fauchez, T., P. Dubuisson, C. Cornet, F. Szczap, A. Garnier, J. Pelon, and K. Meyer (2015), Impacts of cloud heterogeneities on cirrus optical properties retrieved from space-based thermal infrared radiometry, *Atmos. Meas. Tech.*, *8*, 633–647.
Field, P., R. Wood, P. Brown, P. H. Kaye, E. Hirst, R. Greenaway, and J. Smith (2003), Ice particle interarrival times measured with a fast FSSP, *J. Atmos. Oceanic Technol.*, *20*(2), 249–261.
Garnier, A., J. Pelon, P. Dubuisson, M. Faivre, O. Chomette, N. Pascal, and D. P. Kratz (2012), Retrieval of cloud properties using CALIPSO imaging infrared radiometer. Part I: Effective emissivity and optical depth, *J. Appl. Meteorol. Climatol.*, *51*(7), 1407–1425.
Garnier, A., J. Pelon, M. A. Vaughan, D. M. Winker, C. R. Trepte, and P. Dubuisson (2015), Lidar multiple scattering factors inferred from CALIPSO lidar and IIR retrievals of semi-transparent cirrus cloud optical depth over ocean, *Atmos. Meas. Tech.*, *8*, 2759–2774.
Guignard, A., C. Stubenrauch, A. Baran, and R. Armante (2012), Bulk microphysical properties of semi-transparent cirrus from AIRS: A six year global climatology and statistical analysis in synergy with geometrical profiling data from CloudSat-CALIPSO, *Atmos. Chem. Phys.*, *12*(1), 503–525.
Heymsfield, A. J., and J. Iaquinta (2000), Cirrus crystal terminal velocities, *J. Atmos. Sci.*, *57*(7), 916–938.
Heymsfield, A. J., C. Schmitt, and A. Bansemer (2013), Ice cloud particle size distributions and pressure-dependent terminal velocities from in situ observations at temperatures from 0 to $-86°$C, *J. Atmos. Sci.*, *70*(12), 4123–4154.
Hioki, S., P. Yang, B. A. Baum, S. Platnick, K. G. Meyer, M. D. King, and J. Riedi (2016), Degree of ice particle surface roughness inferred from polarimetric observations, *Atmos. Chem. Phys.*, *16*(12), 7545–7558.
Holz, R. E. et al. (2016), Resolving ice cloud optical thickness biases between CALIOP and MODIS using infrared retrievals, *Atmos. Chem. Phys.*, *16*(8), 5075–5090.
Hong, G., P. Yang, B. A. Baum, A. J. Heymsfield, and K.-M. Xu (2009), Parameterization of shortwave and longwave radiative properties of ice clouds for use in climate models, *J. Clim.*, *22*(23), 6287–6312.
Hu, Y., et al. (2009), CALIPSO/CALIOP cloud phase discrimination algorithm, *J. Atmos. Oceanic Technol.*, *26*(11), 2293–2309.
Hu, Y.-X., D. Winker, P. Yang, B. Baum, L. Poole, and L. Vann (2001), Identification of cloud phase from PICASSO-CENA lidar depolarization: A multiple scattering sensitivity study, *J. Quant. Spectrosc. Radiat. Transfer*, *70*(4), 569–579.
Illingworth, A. J., et al. (2015), The EarthCARE satellite: The next step forward in global measurements of clouds, aerosols, precipitation, and radiation, *Bull. Am. Meteorol. Soc.*, *96*(8), 1311–1332.
Inoue, T. (1987), A cloud type classification with NOAA 7 split-window measurements, *J. Geophys. Res.*, *92*(D4), 3991–4000.
Iwabuchi, H., P. Yang, K. Liou, and P. Minnis (2012), Physical and optical properties of persistent contrails: Climatology and interpretation, *J. Geophys. Res.*, *117*, D06215, doi:10.1029/2011JD017020.
Iwabuchi, H., S. Yamada, S. Katagiri, P. Yang, and H. Okamoto (2014), Radiative and microphysical properties of cirrus cloud inferred from infrared measurements made by the Moderate Resolution Imaging Spectroradiometer (MODIS). Part I: Retrieval method, *J. Appl. Meteorol. Climatol.*, *53*(5), 1297–1316.
Iwabuchi, H., M. Saito, Y. Tokoro, N. S. Putri, and M. Sekiguchi (2016), Retrieval of radiative and microphysical properties of cloud from multispectral infrared measurements, *Prog. Earth Planet. Sci.*, *3*(1), 32.
Josset, D., J. Pelon, A. Garnier, Y. Hu, M. Vaughan, P.-W. Zhai, R. Kuehn, and P. Lucker (2012), Cirrus optical depth and lidar ratio retrieval from combined CALIPSO-CloudSat observations using ocean surface echo, *J. Geophys. Res.*, *117*, D05207, doi:10.1029/2011JD016959.
Key, J. R., P. Yang, B. A. Baum, and S. L. Nasiri (2002), Parameterization of shortwave ice cloud optical properties for various particle habits, *J. Geophys. Res.*, *107*, 4181, doi:10.1029/2001JD000742.
Klett, J. D. (1995), Orientation model for particles in turbulence, *J. Atmos. Sci.*, *52*(12), 2276–2285.
Lawson, R. (2011), Effects of ice particles shattering on the 2D-S probe, *Atmos. Meas. Tech.*, *4*(7), 1361–1381.
Lawson, R. P., B. Baker, B. Pilson, and Q. Mo (2006), In situ observations of the microphysical properties of wave, cirrus, and anvil clouds. Part II: Cirrus clouds, *J. Atmos. Sci.*, *63*, 3186–3203.
Liou, K. N., and P. Yang (2016), *Light Scattering by Ice Crystals: Fundamentals and Applications*, Cambridge Univ. Press, Cambridge, U. K.
Magee, N., A. Miller, M. Amaral, and A. Cumiskey (2014), Mesoscopic surface roughness of ice crystals pervasive across a wide range of ice crystal conditions, *Atmos. Chem. Phys.*, *14*(22), 12,357–12,371.
Nakajima, T., and M. D. King (1990), Determination of the optical thickness and effective particle radius of clouds from reflected solar radiation measurements. Part I: Theory, *J. Atmos. Sci.*, *47*(15), 1878–1893.
Nakajima, T., and M. Tanaka (1986), Matrix formulations for the transfer of solar radiation in a plane-parallel scattering atmosphere, *J. Quant. Spectrosc. Radiat. Transfer*, *35*(1), 13–21.
Nakajima, T., and M. Tanaka (1988), Algorithms for radiative intensity calculations in moderately thick atmospheres using a truncation approximation, *J. Quant. Spectrosc. Radiat. Transfer*, *40*(1), 51–69.

Nakajima, T., M. Tsukamoto, Y. Tsushima, A. Numaguti, and T. Kimura (2000), Modeling of the radiative process in an atmospheric general circulation model, *Appl. Opt.*, *39*(27), 4869–4878.
Newman, S., J. Smith, M. Glew, S. Rogers, and J. Taylor (2005), Temperature and salinity dependence of sea surface emissivity in the thermal infrared, *Q. J. R. Meteorol. Soc.*, *131*(610), 2539–2557.
Noel, V., and H. Chepfer (2004), Study of ice crystal orientation in cirrus clouds based on satellite polarized radiance measurements, *J. Atmos. Sci.*, *61*(16), 2073–2081.
Noel, V., and K. Sassen (2005), Study of planar ice crystal orientations in ice clouds from scanning polarization lidar observations, *J. Appl. Meteorol.*, *44*(5), 653–664.
Noel, V., and H. Chepfer (2010), A global view of horizontally oriented crystals in ice clouds from Cloud-Aerosol Lidar and Infrared Pathfinder Satellite Observation (CALIPSO), *J. Geophys. Res.*, *115*, D00H23, doi:10.1029/2009JD012365.
Parol, F., J. Buriez, G. Brogniez, and Y. Fouquart (1991), Information content of AVHRR channels 4 and 5 with respect to the effective radius of cirrus cloud particles, *J. Appl. Meteorol.*, *30*(7), 973–984.
Platnick, S., et al. (2017), The MODIS cloud optical and microphysical products: Collection 6 updates and examples from Terra and Aqua, *IEEE Trans. Geosci. Remote Sens.*, *55*, 502–525.
Pfalzgraff, W., R. Hulscher, and S. Neshyba (2010), Scanning electron microscopy and molecular dynamics of surfaces of growing and ablating hexagonal ice crystals, *Atmos. Chem. Phys.*, *10*(6), 2927–2935.
Pruppacher, H., and J. Klett (1997), *Microphysics of Clouds and Precipitation: With an Introduction to Cloud Chemistry and Cloud Electricity*, 954 pp., Springer, New York.
Reichardt, J, S. Reichardt, M. Hess, and T. J. McGee (2002), Correlations among the optical properties of cirrus-cloud particles: Microphysical interpretation, *J. Geophys. Res. Atmos.*, *107*(D21), 15,185–15,199.
Rienecker, M. M., et al. (2011), MERRA: NASA's modern-era retrospective analysis for research and applications, *J. Clim.*, *24*, 3624–3648.
Rodgers, C. D. (2000), *Inverse Methods for Atmospheric Sounding: Theory and Practice*, vol. 2, 238 pp., World Scientific Publ. Co., Singapore.
Sassen, K. (1980), Remote sensing of planar ice crystal fall attitudes, *J. Meteorol. Soc. Jpn*, *58*(5), 422–429.
Sassen, K. (1991), The polarization lidar technique for cloud research: A review and current assessment, *Bull. Am. Meteorol. Soc.*, *72*(12), 1848–1866.
Sassen, K., and S. Benson (2001), A midlatitude cirrus cloud climatology from the facility for atmospheric remote sensing. Part II: Microphysical properties derived from lidar depolarization, *J. Atmos. Sci.*, *58*(15), 2103–2112.
Sassen, K., and J. M. Comstock (2001), A midlatitude cirrus cloud climatology from the facility for atmospheric remote sensing. Part III: Radiative properties, *J. Atmos. Sci.*, *58*(15), 2113–2127.
Sassen, K., Z. Wang, and D. Liu (2008), Global distribution of cirrus clouds from CloudSat/Cloud-Aerosol Lidar and Infrared Pathfinder Satellite Observations (CALIPSO) measurements, *J. Geophys. Res.*, *113*, D00A12, doi:10.1029/2008JD009972.
Seemann, S. W., E. E. Borbas, R. O. Knuteson, G. R. Stephenson, and H.-L. Huang (2008), Development of a global infrared land surface emissivity database for application to clear sky sounding retrievals from multispectral satellite radiance measurements, *J. Appl. Meteorol. Climatol.*, *47*(1), 108–123.
Seifert, P., A. Ansmann, D. Müller, U. Wandinger, D. Althausen, A. J. Heymsfield, S. T. Massie, and C. Schmitt (2007), Cirrus optical properties observed with lidar, radiosonde, and satellite over the tropical Indian Ocean during the aerosol-polluted northeast and clean maritime southwest monsoon, *J. Geophys. Res.*, *112*, D17205, doi:10.1029/2006JD008352.
Sekiguchi, M., and T. Nakajima (2008), A k-distribution-based radiation code and its computational optimization for an atmospheric general circulation model, *J. Quant. Spectrosc. Radiat. Transfer*, *109*(17), 2779–2793.
Sourdeval, O., L. C-Labonnote, A. J. Baran, and G. Brogniez (2015), A methodology for simultaneous retrieval of ice and liquid water cloud properties. Part I: Information content and case study, *Q. J. R. Meteorol. Soc.*, *141*(688), 870–882.
Stephens, G. L., S.-C. Tsay, P. W. Stackhouse Jr., and P. J. Flatau (1990), The relevance of the microphysical and radiative properties of cirrus clouds to climate and climatic feedback, *J. Atmos. Sci.*, *47*(14), 1742–1754.
Stephens, G. L., et al. (2002), The CloudSat mission and the A-Train: A new dimension of space-based observations of clouds and precipitation, *Bull. Am. Meteorol. Soc.*, *83*(12), 1771–1790.
Tsutsumi, Y., K. Mori, T. Hirahara, M. Ikegami, and T. J. Conway, (2009), Technical report of global analysis method for major greenhouse gases by the world data center for greenhouse gases, GAW Rep. No. 184 (WMO/TD No. 1473), 29 pp., Geneva, Switzerland.
Ulanowski, Z., P. H. Kaye, E. Hirst, R. Greenaway, R. J. Cotton, E. Hesse, and C. T. Collier (2014), Incidence of rough and irregular atmospheric ice particles from small ice detector 3 measurements, *Atmos. Chem. Phys.*, *14*(3), 1649–1662.
van Diedenhoven, B., B. Cairns, I. Geogdzhayev, A. Fridlind, A. Ackerman, P. Yang, and B. Baum (2012), Remote sensing of ice crystal asymmetry parameter using multi-directional polarization measurements—Part 1: Methodology and evaluation with simulated measurements, atmos, *Atmos. Meas. Tech.*, *5*, 2361–2374.
van Diedenhoven, B., A. M. Fridlind, B. Cairns, and A. S. Ackerman (2014), Variation of ice crystal size, shape, and asymmetry parameter in tops of tropical deep convective clouds, *J. Geophys. Res. Atmos.*, *119*(20), 11–809.
Várnai, T., and A. Marshak (2007), View angle dependence of cloud optical thicknesses retrieved by moderate resolution imaging spectroradiometer (MODIS), *J. Geophys. Res.*, *112*, D06203, doi:10.1029/2005JD006912.
Vaughan, M. A., S. A. Young, D. M. Winker, K. A. Powell, A. H. Omar, Z. Liu, Y. Hu, and C. A. Hostetler (2004), Fully automated analysis of space-based lidar data: An overview of the CALIPSO retrieval algorithms and data products, in *Laser Radar Techniques for Atmospheric Sensing, Proceedings of SPIE*, vol. 5575, edited by U. N. Singh, pp. 16–30, International Society for Optical Engineering, Maspalomas, Spain.
Wan, Z., and Z.-L. Li (1997), A physics-based algorithm for retrieving land-surface emissivity and temperature from EOS/MODIS data, *IEEE Trans. Geosci. Remote Sens.*, *35*(4), 980–996.
Wang, C., S. Platnick, Z. Zhang, K. Meyer, and P. Yang (2016), Retrieval of ice cloud properties using an optimal estimation algorithm and MODIS infrared observations: 1. Forward model, error analysis, and information content, *J. Geophys. Res. Atmos.*, *121*, 5809–5826, doi:10.1002/2015JD024526.
Winker, D. M., M. A. Vaughan, A. Omar, Y. Hu, K. A. Powell, Z. Liu, W. H. Hunt, and S. A. Young (2009), Overview of the CALIPSO mission and CALIOP data processing algorithms, *J. Atmos. Oceanic Technol.*, *26*(11), 2310–2323.
Wiscombe, W. (1977), The delta-M method: Rapid yet accurate radiative flux calculations for strongly asymmetric phase functions, *J. Atmos. Sci.*, *34*(9), 1408–1422.
Yang, P., and K. Liou (1996), Geometric-optics–integral-equation method for light scattering by nonspherical ice crystals, *Appl. Opt.*, *35*(33), 6568–6584.
Yang, P., and K. Liou (1998), Single-scattering properties of complex ice crystals in terrestrial atmosphere, *Contr. Atmos. Phys.*, *71*, 223–248.

Yang, P., G. Hong, G. W. Kattawar, P. Minnis, and Y. Hu (2008), Uncertainties associated with the surface texture of ice particles in satellite-based retrieval of cirrus clouds: Part II effect of particle surface roughness on retrieved cloud optical thickness and effective particle size, *IEEE Trans. Geosci. Remote Sens.*, *46*(7), 1948–1957.
Yi, B., P. Yang, B. A. Baum, T. L'Ecuyer, L. Oreopoulos, E. J. Mlawer, A. J. Heymsfield, and K.-N. Liou (2013), Influence of ice particle surface roughening on the global cloud radiative effect, *J. Atmos. Sci.*, *70*(9), 2794–2807.
Yoshida, R., H. Okamoto, Y. Hagihara, and H. Ishimoto (2010), Global analysis of cloud phase and ice crystal orientation from cloud-aerosol lidar and infrared pathfinder satellite observation (CALIPSO) data using attenuated backscattering and depolarization ratio, *J. Geophys. Res.*, *115*, D00H32, doi:10.1029/2009JD012334.
Young, S. A., and M. A. Vaughan (2009), The retrieval of profiles of particulate extinction from Cloud-Aerosol Lidar Infrared Pathfinder Satellite Observations (CALIPSO) data: Algorithm description, *J. Atmos. Oceanic Technol.*, *26*(6), 1105–1119.
Zhang, Z., S. Platnick, P. Yang, A. K. Heidinger, and J. M. Comstoc (2010), Effects of ice particle size vertical inhomogeneity on the passive remote sensing of ice clouds, *J. Geophys. Res.*, *115*, D17203, doi:10.1029/2010JD013835.
Zhou, C., and P. Yang (2015), Backscattering peak of ice cloud particles, *Opt. Express*, *23*(9), 11,995–12,003.
Zhou, C., P. Yang, A. E. Dessler, Y. Hu, and B. A. Baum (2012), Study of horizontally oriented ice crystals with CALIPSO observations and comparison with Monte Carlo radiative transfer simulations, *J. Appl. Meteorol. Climatol.*, *51*(7), 1426–1439.